

RESEARCH ARTICLE

Computational Model of Ca^{2+} Wave Propagation in Human Retinal Pigment Epithelial ARPE-19 Cells

Iina Vainio^{1,2*}, Amna Abu Khamidakh^{1,2}, Michelangelo Paci^{1,2}, Heli Skottman³, Kati Juuti-Uusitalo³, Jari Hyttinen^{1,2}, Soile Nymark^{1,2}

1 Department of Electronics and Communications Engineering, Tampere University of Technology, Tampere, Finland, **2** Institute of Biosciences and Medical Technology, Tampere University of Technology, Tampere, Finland, **3** Institute of Biosciences and Medical Technology, University of Tampere, Tampere, Finland

* iina.vainio@tut.fi



CrossMark
click for updates

Abstract

OPEN ACCESS

Citation: Vainio I, Abu Khamidakh A, Paci M, Skottman H, Juuti-Uusitalo K, Hyttinen J, et al. (2015) Computational Model of Ca^{2+} Wave Propagation in Human Retinal Pigment Epithelial ARPE-19 Cells. PLoS ONE 10(6): e0128434. doi:10.1371/journal.pone.0128434

Academic Editor: Zsolt Ablonczy, Medical University of South Carolina, UNITED STATES

Received: October 24, 2014

Accepted: April 27, 2015

Published: June 12, 2015

Copyright: © 2015 Vainio et al. This is an open access article distributed under the terms of the Creative Commons Attribution License, which permits unrestricted use, distribution, and reproduction in any medium, provided the original author and source are credited.

Data Availability Statement: All relevant data are within the paper.

Funding: This study was financially supported by the Academy of Finland (grant numbers 252225, 260375, 218050 and 137801), TEKES- the finnish funding agency for innovation (Human Spare Part Project), and Doctoral Programme of the President of the Tampere University of Technology. The funders had no role in study design, data collection and analysis, decision to publish, or preparation of the manuscript.

Objective

Computational models of calcium (Ca^{2+}) signaling have been constructed for several cell types. There are, however, no such models for retinal pigment epithelium (RPE). Our aim was to construct a Ca^{2+} signaling model for RPE based on our experimental data of mechanically induced Ca^{2+} wave in the *in vitro* model of RPE, the ARPE-19 monolayer.

Methods

We combined six essential Ca^{2+} signaling components into a model: stretch-sensitive Ca^{2+} channels (SSCCs), P_2Y_2 receptors, IP_3 receptors, ryanodine receptors, Ca^{2+} pumps, and gap junctions. The cells in our epithelial model are connected to each other to enable transport of signaling molecules. Parameterization was done by tuning the above model components so that the simulated Ca^{2+} waves reproduced our control experimental data and data where gap junctions were blocked.

Results

Our model was able to explain Ca^{2+} signaling in ARPE-19 cells, and the basic mechanism was found to be as follows: 1) Cells near the stimulus site are likely to conduct Ca^{2+} through plasma membrane SSCCs and gap junctions conduct the Ca^{2+} and IP_3 between cells further away. 2) Most likely the stimulated cell secretes ligand to the extracellular space where the ligand diffusion mediates the Ca^{2+} signal so that the ligand concentration decreases with distance. 3) The phosphorylation of the IP_3 receptor defines the cell's sensitivity to the extracellular ligand attenuating the Ca^{2+} signal in the distance.

Competing Interests: The authors have declared that no competing interests exist.

Conclusions

The developed model was able to simulate an array of experimental data including drug effects. Furthermore, our simulations predict that suramin may interfere ligand binding on P₂Y₂ receptors or accelerate P₂Y₂ receptor phosphorylation, which may partially be the reason for Ca²⁺ wave attenuation by suramin. Being the first RPE Ca²⁺ signaling model created based on experimental data on ARPE-19 cell line, the model offers a platform for further modeling of native RPE functions.

Introduction

Epithelial tissue covers and lines all internal and external body surfaces. These cell layers have multiple functions depending on their location, and many of these functions are controlled by Ca²⁺ activity[1]. Retinal pigment epithelium (RPE), a monolayer of pigmented polarized cells, is crucial for the maintenance of visual functions. Located in the back of the eye between photoreceptors and choriocapillaries, RPE forms a vital part of the blood-retinal barrier (BRB)[2]. The physiology of RPE is tightly coupled with the activity of the various ion channels, such as Ca²⁺ channels that are associated with several important RPE functions including transepithelial transport of ions and water, dark adaption of photoreceptor activity, phagocytosis, secretion, and differentiation[3]. In RPE, as well as in other epithelia, local deformation of the cell membrane initiates a significant Ca²⁺ wave [4–6]. Such deformation of the cell membrane can occur in clinically important pathological conditions such as retinal tear resulting from complications after photodynamic therapy[7], intravitreal bevacizumab injection[8], or intravitreal pegaptanib injection[9]. Intercellular Ca²⁺ signaling is also linked to the initial stages of wound repair: excessive mechanical stimulation causes cell death and thus initiates Ca²⁺ waves that create Ca²⁺ gradients which play an important role in cell migration[1]. In addition, Ca²⁺ waves also regulate the local transepithelial ion transport to maintain the spatial ion gradients across the epithelium[1]. We recently demonstrated in RPE that an easily induced and repeatable Ca²⁺ wave could be produced by mechanical stimulation[5]. This provides an experimental way to study Ca²⁺ activity in the epithelial monolayer.

In silico models of various cellular processes are becoming an increasingly important part of biological research, including drug discovery and toxicology studies. The importance of this was recently emphasized in a review of cardiotoxicity testing [10]. Computational models of Ca²⁺ signaling, specifically, have been developed for many cell types including pancreatic and parotid acinar cells[11], astrocytes[12], and hepatocytes[13]. Epithelial Ca²⁺ signaling, however, differs from other cell types because the epithelium forms a highly polarized cell monolayer that comprises organized apical and basal cell membranes. The epithelial cells are tightly connected with tight junctions and gap junctions between the cells[14]. At present, there are only a few epithelial Ca²⁺ signaling models available, for example for the urothelial monolayer[15] and for the airway epithelium[16]. RPE has many unique functions compared to other epithelia as it supports the complex processes of vision. Indeed, in the treatment of many eye diseases, RPE is either the drug target or it hinders drug penetration and provides a barrier between most of the eye and the blood stream. Hence, computational models of the functions of RPE, including Ca²⁺ dynamics, are well warranted.

The aim of this study, therefore, is to provide a deeper understanding of the study of Ca²⁺ activity by introducing a detailed computational model of RPE Ca²⁺ dynamics. The computational model described in this paper is based on our experimental data on a mechanically

induced Ca^{2+} wave in ARPE-19 cells, a commercial immortalized human RPE cell line that is widely used to assess RPE cell functions *in vitro* [17–19], regardless of its limitations in cellular morphology, organization and function [20].

The computational model is mostly based on the experimental data of Abu Khamidakh et al. 2013[5]. In addition, the model comprises our new unpublished α -glycyrrhetic acid (GA)-suramin-treated data. We constructed the model by combining previously published cell Ca^{2+} dynamics model components of P_2Y_2 receptors [21], inositol 1,4,5-trisphosphate (IP_3) receptors [22], ryanodine receptors [23], Ca^{2+} pumps and gap junctions to a new model component of mechanical stretch. Furthermore, we connected the epithelial cells to each other in the model to enable the diffusion of the molecules and propagation of the stretch. We developed the model based on two experimental data sets: the GA-treated data, where gap junctions (GJs) were blocked by α -glycyrrhetic acid and untreated control data, where GJs define the connections between the cells. The varying conditions the cells are exposed to due to the mechanical stimulation were modeled by defining three location-specific variables: stretch, extracellular ligand concentration, and IP_3 receptor phosphorylation rate. In addition, we validated the model by simulating the combined blocking effect of GJs and P_2 receptors by GA and suramin. This way, we obtained the first RPE Ca^{2+} signaling model, and we could reveal a deeper understanding of Ca^{2+} activity.

Materials and Methods

Experimental data

In this study, the experimental data of Abu Khamidakh et al. 2013[5] was complemented with new experimental data. Passage numbers for confluent cultures of human RPE immortalized cells (ARPE-19 cell line [ATCC Manassas, VA, U.S.A.]) were p. 23, 24, 30 for GA-treated data set, p. 23, 24, 28, 30 for control data set and p. 29, 30, 31 for GA-suramin-treated data set. These ARPE-19 cultures were used for Ca^{2+} imaging, by loading them with the Ca^{2+} -sensitive dye fura-2-acetoxymethyl ester. Single cell mechanical stimulation, membrane perforation of one cell, was induced with a glass micropipette. The intracellular Ca^{2+} concentration transient travelled over the ARPE-19 monolayer starting from the mechanically stimulated (MS) cell, and spreading to the neighboring (NB) cells (Fig 1). The NB cells immediately surrounding the MS cell were defined as the first NB cell layer (NB layer 1 = NB_1); cells immediately surrounding the first layer were defined as the second NB layer (NB layer 2 = NB_2) and so on. The ratio of the emitted fluorescence intensities resulting from excitation at 340 and 380 nm ($\text{F}_{340}/\text{F}_{380}$) was determined for each cell after background correction. Normalized fluorescence (NF), which reflects the changes in intracellular Ca^{2+} concentration, was then obtained by dividing the fluorescence value by the mean fluorescence value before the mechanical stimulation.[5] The experimental work produced data in NF units. The computational model, however, is presented in absolute calcium concentrations. Due to the lack of absolute reference we consider the model predictions only relative.

Three data sets were simulated with the model. Firstly, in the GA-treated data set the gap junctions (GJs) were blocked by α -glycyrrhetic acid (GA) (Sigma-Aldrich, St. Louis, MO, USA). Secondly, the model was verified with an untreated control data set that was based on the previous model—only the GJ model component was added. Thirdly, the model was applied to predict a combined blocking effect of GA and P_2 receptor blocker suramin (Sigma-Aldrich) with GA-suramin-treated data set. Each data set was averaged from at least three separate experiments.

The experiments with GA-suramin-treated ARPE-19 cells were not included in the original paper of Abu Khamidakh et al. 2013[5]. The experimental details concerning the ARPE-19 cells as well as the experimental solutions, infrastructure, and protocols are presented in[5] with the following exception: the cells were incubated in a solution containing 30 μM GA

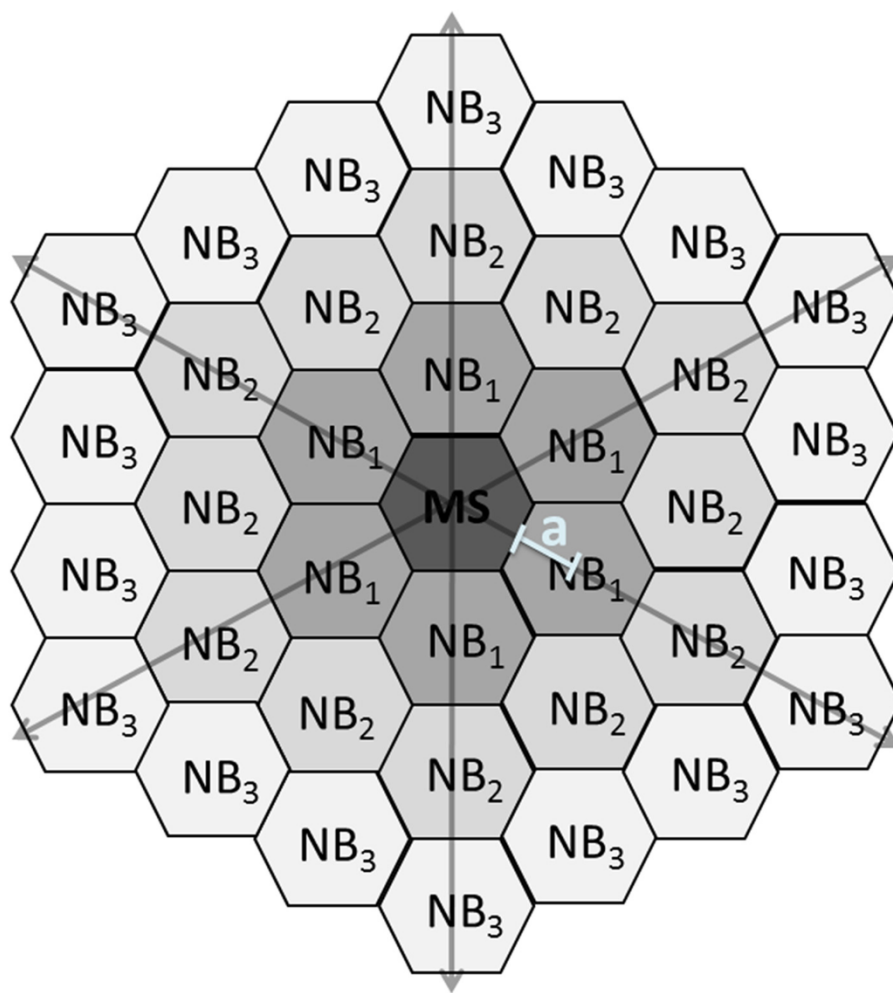


Fig 1. Numbering of the cell layers. Schematic representation of the location of the mechanically stimulated (MS) cell with respect to the neighboring (NB) cell layers: NB₁ is the first layer which is in direct contact with the MS cell; NB₂ is the second layer which is in direct contact with NB₁, and so forth. White line segment marks an apothem (a) of a hexagon.

doi:10.1371/journal.pone.0128434.g001

(incubation time 30 min) and 50 μM suramin (incubation time 25 min) prior to mechanical stimulation. To receive representative data for each NB layer, the raw data was averaged so that the NF graphs were aligned by the starting time of mechanical stimulation, and the mean values were calculated for each NB with a one-second sampling rate. This was previously done for the control data set[5], but the averaging was performed also here for the GA-treated and GA-suramin-treated data sets.

Indirect immunofluorescence staining. ARPE-19 cells (p. 24, 27, 44, three cover slips from each passage) were cultured on glass coverslips for two days. For immunofluorescence staining, the samples were washed three times with PBS and fixed for 15 min with 4% paraformaldehyde (pH 7.4; Sigma-Aldrich) at room temperature (RT). After three subsequent washes with PBS, the samples were permeabilizing by a 15 min incubation in 0.1% Triton X-100 in PBS (Sigma-Aldrich) at RT. This was followed again by three PBS washes, after which the samples were incubated with 3% bovine serum albumin (BSA; Sigma-Aldrich) at RT for 1 h. Primary antibody Zonula Occludens (ZO-1) 1:100 (33–9100, Life Technologies) was diluted in 3% BSA PBS and incubated for 1 h at RT. Samples were then washed four times with PBS, and

followed by 1h incubation at RT with secondary antibody donkey anti-mouse Alexa Fluor 568 (A10037, Life Technologies) diluted 1:400 in 3% BSA in PBS. The washes with PBS were repeated again and nuclei were stained with 4', 6' diamidino-2-phenylidole (DAPI) included in the mounting medium (P36935, Life Technologies).

Confocal microscopy and image processing. Zeiss LSM780 LSCM on inverted Zeiss Cell Observer microscope (Zeiss, Jena, Germany) with Plan-Apochromat 63x/1.4 oil immersion objective was used for confocal microscopy. Voxel size was set to $x = y = 66\text{nm}$ and $z = 200\text{nm}$, pixel stacks were set to 1024x1024, and approximately 50–80 slices were acquired with line average of 2. DAPI and Alexa-568 were excited with 405nm and 561nm lasers and detected with emission windows of 410–495nm and 570–642nm, respectively. The images saved in czi format were processed with ImageJ (Rasband, W.S., ImageJ, U. S. National Institutes of Health, Bethesda, Maryland, USA, <http://imagej.nih.gov/ij/>, 1997–2014.) and assembled using Adobe Photoshop CS6 (Adobe Systems, San Jose, USA).

Construction of the model

The Ca^{2+} model was constructed by combining six subcellular model components that included the stretch component designed in this study and the P_2Y_2 receptor models of Lemon et al. 2003[21], the IP_3 receptor type 3 (IP_3R_3) of LeBeau et al. 1999[22], and the ryanodine receptor (RyR) of Keizer & Levine 1996[23]. The GJ model component connected the neighboring cells. These model components with corresponding numbering and their rationale, hypothesized Ca^{2+} wave propagation mechanisms as well as model equations (see chapter [Detailed model equations](#)) that were used for the NB layers and data sets are summarized in [Table 1](#). The basis for the mathematical implementation is presented in [Fig 2](#) as a schematic model.

Parameters and parameterization

The model parameters are represented in [Table 2](#) and the parameters specific for each NB layer in [Table 3](#). Most of the parameters were adopted from the models of Lemon et al. 2003[21], LeBeau et al. 1999[22], and Keizer & Levine 1996[23]. Typically, the volumes of ARPE-19 cells [5,24,25] and RPE cells[26,27] are variable. The cell width was approximated to be $14\mu\text{m}$ from the corner-to-corner of a hexagon and the height was $12\mu\text{m}$ [5]. The cytoplasmic volume was approximated to be about 70% of the total cell volume[28]. Thus, a cytoplasmic volume (v) of $1.07 \cdot 10^{-15} \text{ m}^3$ was used in the simulations. The initial values, the values at time of mechanical stimulation, were taken mostly from the model of Lemon et al. 2003[21]. The initial value $0.12\mu\text{M}$ for intracellular Ca^{2+} concentration ($[\text{Ca}^{2+}]_i$) is an arbitrary value approximating the baseline Ca^{2+} concentration determined from GA-treated data set for $\text{NB}_5\text{-NB}_{10}$ layers using Matlab SimBiology Toolbox.

The rest of the parameters were fitted with Matlab SimBiology Parameter Fit Task: First, the parameter values, excluding SSCC and GJ model components, were fitted with GA-treated data set in NB5 layer. This layer has in general the largest Ca^{2+} response from those NB layers that do not experience any stretch due to mechanical stimulation, according to our assumption. Secondly, the SSCC model component parameters, excluding the location-specific stretch (θ) parameter (see below), were fitted with the same GA-treated data set in NB1 layer that is assumed to have the largest stretch. These values were then used in all simulations for all data sets and NB layers. For the control data set with gap junctions, all other parameters were kept unchanged but the GJ related diffusion parameters, $D_{\text{Ca}^{2+}}$, D_{IP_3} , $In_{\text{Ca}^{2+}}$ and In_{IP_3} , were fitted using NB1 layer. As a boundary condition we assumed that there is no outflow of IP_3 and Ca^{2+} outside the epithelium, thus Out_{IP_3} and $Out_{\text{Ca}^{2+}}$ were assigned to be zero.

Table 1. Model design.

Mechanism	Number	Component	Rationale	Equations	NB layer	Data set
Mechanical stimulus applied to MS cell may stretch ARPE-19 cells near the site of stimulation [5] resulting in the opening of SSCCs that conduct Ca^{2+} from the extracellular space to the cytoplasm. It is shown that ARPE-19 cells can secrete ligand to the extracellular space as a response to stimuli [38].	I	Stretch-sensitive Ca^{2+} channel (SSCC)	Cultured rat RPE expresses SSCCs on plasma membrane [4,53]. In ARPE-19 $[\text{Ca}^{2+}]_i$ wave was seen in NB ₁ -NB ₄ layers even when the ER was depleted[5], indicating a Ca^{2+} influx mechanism independent of the ER, possibly the SSCCs.	7–9 ^a	1–4	GA-treated, Control, GA-suramin-treated
The ligand, likely ATP or UTP [3,30,38,54], interacts with G-protein coupled purinergic receptor type P ₂ Y ₂ on the cell membrane leading to the production of inositol 1,4,5-trisphosphate (IP ₃) to the cytoplasm in a ligand concentration dependent manner.	II	Purinergic P ₂ Y ₂ receptor (P ₂ Y ₂)	The presence of P ₂ Y ₂ receptors has been shown in cultured human RPE[30], bovine and human fetal RPE as well as in Long-Evans rats[55]	10–16 ^b	1–10	GA-treated, Control, GA-suramin-treated ^e
IP ₃ diffuses across the cytoplasm to the endoplasmic reticulum (ER), where it interacts with IP ₃ R ₃ resulting in a release of Ca^{2+} from the ER[22].	III	IP ₃ receptor type 3 (IP ₃ R ₃)	Currently there is no direct evidence about the subtype of IP ₃ R expressed in ARPE-19. Hence, the data from other epithelia [56], [57], and[58] and an epithelial model [16] was utilized to choose the subtype 3 (IP ₃ R ₃).	17–21 ^c	1–10	GA-treated, Control, GA-suramin-treated
As the cytoplasmic Ca^{2+} concentration increases, RyRs become activated releasing more Ca^{2+} to the cytoplasm from the ER[23].	IV	Ryanodine receptor (RyR)	RyRs, located on the membrane of ER participate in Ca^{2+} signaling in rat RPE[4], and ARPE-19[51].	22–24 ^d	1–10	GA-treated, Control, GA-suramin-treated
The cytoplasmic Ca^{2+} concentration is decreased by the pumping activities of SERCA and PMCA. IP ₃ is degraded in the cytoplasm. Ca^{2+} leak currents maintain the cytoplasmic Ca^{2+} baseline level.	V	Sarco/endoplasmic reticulum ATPase (SERCA), plasma membrane Ca^{2+} ATPase (PMCA), Leak	The presence of SERCA has been shown by blocking it to deplete the ER from Ca^{2+} in ARPE-19 cells[5] and rat RPE [53]. PMCA has been identified on the plasma membrane of cultured human RPE[59].	25	1–10	GA-treated, Control, GA-suramin-treated
GJs form intercellular connections between neighboring cells allowing diffusion of Ca^{2+} and IP ₃ between the NB layers.	VI	Gap junction (GJ)	GJs form intercellular connections in ARPE-19[5], and rat RPE[4,60] enabling Ca^{2+} wave to spread over the monolayer.	26–28	1–10	Control

^aDesigned in this study

^bLemon et al. 2003[21]

^cLeBeau et al. 1999[22]

^dKeizer & Levine 1996[23]

^eParameter values of k_p modified

Hypothesized mechanisms and model components for Ca^{2+} wave propagation after mechanical stimulation with corresponding equations, NB layers, and data sets.

doi:10.1371/journal.pone.0128434.t001

Location-dependent parameters

Three parameters were assumed to vary according to the location of the cell with respect to the MS cell: stretch (θ) activating the stretch-sensitive Ca^{2+} channels (SSCCs), the extracellular ligand concentration ([L])[6,16,29,30], and the phosphorylation rate of IP₃R₃ (α_4)[22]. Ca^{2+}

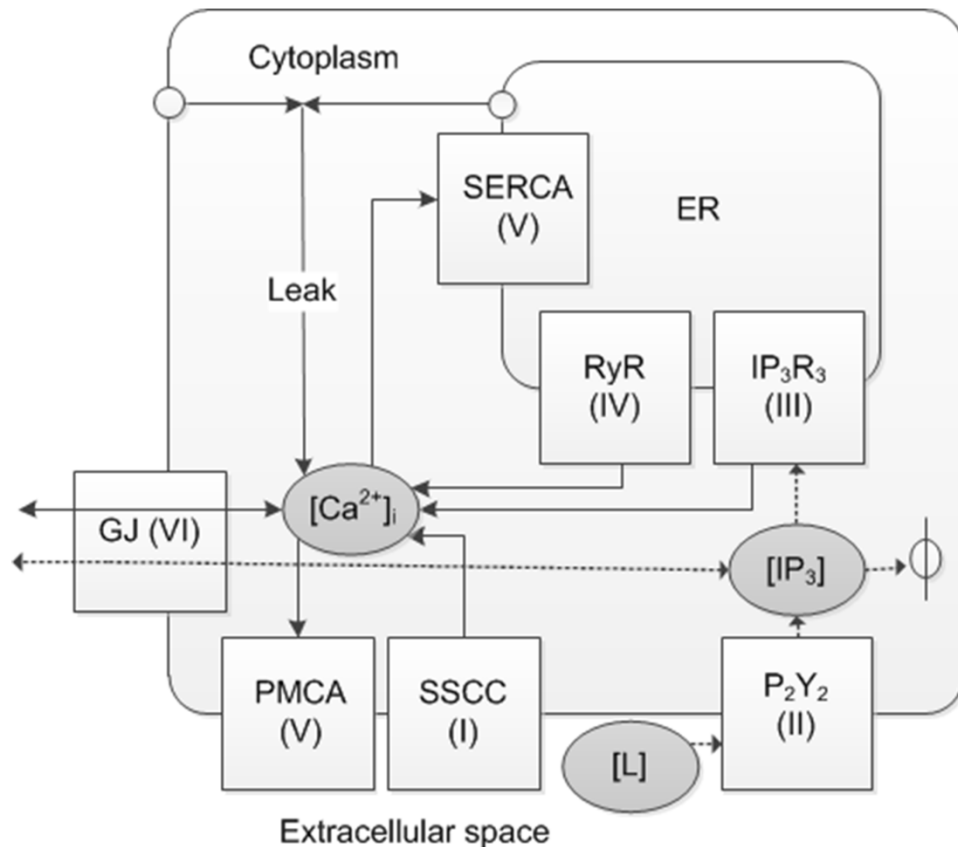


Fig 2. Schematic diagram of the Ca²⁺ signaling model. Solid arrows represent Ca²⁺ fluxes and dashed arrows represent IP₃ dynamics. Roman numerals denote the model components I-VI. Abbreviations: [Ca²⁺]_i = cytosolic Ca²⁺ concentration, [L] = extracellular ligand concentration, [IP₃] = cytosolic IP₃ concentration, SSCC = stretch-sensitive Ca²⁺ channel, P₂Y₂ = purinergic receptor type P₂Y₂, IP₃R₃ = IP₃ receptor type 3, RyR = ryanodine receptor, SERCA = sarco/endoplasmic reticulum Ca²⁺ ATPase, PMCA = plasma membrane Ca²⁺ ATPase, Leak = combinatory Ca²⁺ leak from the extracellular space and the endoplasmic reticulum (ER), GJ = gap junction, ϕ = degradation.

doi:10.1371/journal.pone.0128434.g002

concentration was modeled separately in each NB layer. The distance (x) defines the distance of the NB layer from the MS cell centre that was calculated using the idealized hexagon RPE cell architecture (Fig 1) as

$$x = a2n = \frac{s}{2\tan\left(\frac{180}{6}\right)} 2n, \quad (1)$$

where a is an apothem of the hexagon, 6 is the number of corners in the hexagon, $s = 7\mu\text{m}$ is the length of the hexagon side and $n = 1, 2, 3 \dots 10$ according to the NB layer numbering.

The stretch component was present in cell layers NB1-NB4. Stretch (θ) was parameterized in the GA-treated data set separately for each NB layer. The obtained parameters resulted in an exponentially decaying function corresponding to the decay of an amplitude envelope of a damped wave in a membrane [31]. This function was then used for modeling the stretch

$$\theta = 0.3426e^{-0.105x}, \quad (2)$$

where x is the distance from the MS cell ($R^2 = 0.9878$).

Table 2. Constant parameters and initial conditions.

Parameter	Description	Value	Reference
I Stretch-sensitive Ca²⁺ channels (SSCCs)			
k_{SSCC}	Maximal SSCC flux rate	1.025 $\mu\text{M s}^{-1}$	fitted
k_f	SSCC forward rate constant	0.1382 s^{-1}	fitted
k_b	SSCC backward rate constant	0.04027 s^{-1}	fitted
k_θ	Stretch-relaxation parameter	0.08105 s^{-1}	fitted
II Metabotropic receptor P₂Y₂			
L_0	Bolus extracellular ligand concentration at $x = 0\mu\text{m}$	1310 μM	fitted
D_{ATP}	Diffusion coefficient of A	236 $\mu\text{m}^2 \text{s}^{-1}$	[61]
$[R_T]$	Total number of P ₂ Y ₂ receptors	$2 \cdot 10^4$	[62]
K_1	Unphosphorylated receptor dissociation constant	5 μM	[21]
K_2	Phosphorylated receptor dissociation constant	100 μM	[21]
k_r	Receptor recycling rate	$1.75 \cdot 10^{-4} \text{s}^{-1}$	[21]
k_p	Receptor phosphorylation rate	0.03 s^{-1}	[21]
k_e	Receptor endocytosis rate	$6 \cdot 10^{-3} \text{s}^{-1}$	[21]
ξ	Fraction of mobile receptors	0.85	[21]
$[G_T]$	Total number of G-protein molecules	$1 \cdot 10^5$	[63]
k_{deg}	IP ₃ degradation rate	1.25 s^{-1}	[64]
k_a	G-protein activation rate	0.017 s^{-1}	[21]
k_d	G-protein deactivation rate	0.15 s^{-1}	[21]
$[(PIP_2)_T]$	Total number of PIP ₂ molecules	$5.0 \cdot 10^4$	[21]
r_r	PIP ₂ replenishment rate	0.015 s^{-1}	[21]
δ	G-protein intrinsic activity parameter	$1.238 \cdot 10^{-3}$	[21]
K_3	Dissociation constant for Ca ²⁺ binding to PLC	0.4 μM	[21]
α	Effective signal gain parameter	$2.781 \cdot 10^{-5} \text{s}^{-1}$	[21]
N_a	Avogadro's constant	$6.02252 \cdot 10^{23}$	
V	Volume of the cytoplasmic space	$1.07 \cdot 10^{-15} \text{ m}^3$	see text
III IP₃ receptor type 3 (IP₃R₃)			
α_1	Maximum rate of k_1	40 $\mu\text{M s}^{-1}$	[22]
β_1	[Ca ²⁺] _i for half-maximal k_1	0.8 μM	[22]
k_{-1}	Rate of O to S transition	0.88 s^{-1}	[22]
k_2	Rate of O to I ₁ transition	0.5 s^{-1}	[22]
k_3	Rate of I ₁ to S transition	0.5 s^{-1}	[22]
β_4	[IP ₃] for half-maximal k_4	0.01 μM	[22]
k_5	Rate of I ₂ to S transition	0.02 s^{-1}	[22]
$k_{IP_3R_3}$	Maximum IP ₃ R ₃ flux rate	155.8 $\mu\text{M s}^{-1}$	fitted
IV Ryanodine receptor (RyR)			
K_a	Keizer & Levine dissociation constant	0.37224 μM	[23]
K_b	Keizer & Levine dissociation constant	0.63601 μM	[23]
K_c	Keizer & Levine dissociation constant	0.05714 μM	[23]
k_{RyR}	Maximum RyR flux rate	16.04 $\mu\text{M s}^{-1}$	fitted
V Ca²⁺ pumps and leak current			
V_{Pump}	Maximal pump rate	5.341 $\mu\text{M s}^{-1}$	fitted
K_{Pump}	[Ca ²⁺] _i for half-maximal V_{Pump}	0.5030 μM	fitted
J_{Leak}	Ca ²⁺ leak current	0.1450 $\mu\text{M s}^{-1}$	fitted
VI Gap junctions (GJ)			
$D_{Ca^{2+}}$	Diffusion coefficient of Ca ²⁺ through GJs	512.7 $\mu\text{m}^2 \text{s}^{-1}$	fitted
D_{IP_3}	Diffusion coefficient of IP ₃ through GJs	913.9 $\mu\text{m}^2 \text{s}^{-1}$	fitted

(Continued)

Table 2. (Continued)

Parameter	Description	Value	Reference
$In_{Ca^{2+}}$	Ca^{2+} input to NB1	-0.003320 $\mu M s^{-1}$	fitted
In_{IP_3}	IP_3 input to NB1	0.5771 $\mu M s^{-1}$	fitted
$Out_{Ca^{2+}}$	Ca^{2+} output from NB10	0 $\mu M s^{-1}$	see text
Out_{IP_3}	IP_3 output from NB10	0 $\mu M s^{-1}$	see text
Initial conditions (time 0s)			
[R ^S]	Total number of unphosphorylated surface receptors	17000	[21]
[R ^S _p]	Total number of phosphorylated surface receptors	0	[21]
[G]	Basal number of G-protein molecules	14	[21]
[IP ₃]	Basal IP ₃ concentration	0.01 μM	[21]
[PIP ₂]	Basal number of PIP ₂ molecules	49997	[21]
[Ca ²⁺] _i	Basal cytoplasmic Ca ²⁺ concentration	0.12 μM	see text

Most of the parameters were taken from the models of Lemon et al. 2003[21] for P₂Y₂ receptor, LeBeau et al. 1999[22] for IP₃R₃, and Keizer & Levine 1996[23] for RyR. Reference 'fitted' means that the parameter was optimized in this study.

doi:10.1371/journal.pone.0128434.t002

Ligand diffusion in the extracellular space is modelled according to thin film solution to Fick's diffusion law [32] as follows describing the ligand concentration (L) as a function of time (t)

$$L(x, t) = \frac{L_0}{\sqrt{4\pi D_{ATP} t}} e^{-x^2/(4Dt)}, \quad (3)$$

where L₀ is the initial bolus ligand concentration above the MS cell (at x = 0), D_{ATP} is the diffusion coefficient for ATP, and x describes the NB layer distance from the central MS cell.

IP₃R₃ phosphorylation rate (α_4) used in Eq 21 was fitted separately for each NB layer in GA-treated and control data sets, which resulted in shallowly rising exponential functions with respect to the distance of the cell from the MS cell (x). The equation for GA-treated data

Table 3. Location-dependent parameters with respect to the MS cell.

Parameter	Description	Equation	Range
x	Distance from the MS cell centre	1	From 12.12 μm (NB1) to 121.24 μm (NB10)
θ	Stretch	2 (exponential decay)	From 0.096 (NB1) to 1.014 10^{-6} (NB10)
L	Extracellular ligand concentration	3 (exponential decay)	From 26.14 μM (NB1) to 2.61 μM (NB10)
α_4	IP ₃ R ₃ phosphorylation rate	4 (exponential rise) 5 (exponential rise)	From 0.0413 s^{-1} (NB1) to 0.1548 s^{-1} (NB10) From 0.0333 (NB1) to 0.1503 (NB10)
$J_{GJ,Ca^{2+}}$	Ca^{2+} flux through GJs	26	From 0.049 $\mu M s^{-1}$ (NB1→NB2) to 1.8 10^{-6} $\mu M s^{-1}$ (NB9→NB10)
J_{GJ,IP_3}	IP ₃ flux through GJs	27	From 0.407 $\mu M s^{-1}$ (NB1→NB2) to 0.022 $\mu M s^{-1}$ (NB9→NB10)
A	Area of the cell membranes connecting NB layers	28	From 1512 μm^2 (NB1) to 10584 μm^2 (NB10)

doi:10.1371/journal.pone.0128434.t003

set ($R^2 = 0.9740$) is

$$\alpha_4 = 0.0357e^{0.0121x} \quad (4)$$

and for control data set ($R^2 = 0.9798$)

$$\alpha_4 = 0.0282e^{0.0138x}. \quad (5)$$

Similarly to θ and L , these functions were then used in simulations instead of values from separate fits.

Model simulations

The parameters were fitted with Matlab SimBiology (R2012a, The MathWorks, Natick, MA) to the experimental data using Parameter Fit task, where the maximum iterations was 100. The solver type was ode45 (Dormand-Prince) and the error model was constant error model. The time step in the simulations was set to $\Delta t = 0.1$ seconds.

Sensitivity analysis

Sensitivity analysis was performed to evaluate the uncertainty of selected parameters that were fitted in this study (parameters $k_{IP_3R_3}$, k_{RyR} , V_{Pump} , K_{Pump} , J_{Leak} , In_{IP_3} , $In_{Ca^{2+}}$, D_{IP_3} and D_{IP_3} from [Table 2](#)) or behaved as location-specific parameters (parameters θ , L and α_4 from [Table 3](#)). Values of these parameters were changed -25%, -10%, 0%, +10% and +25% in the model including all the model components I-VI for the control data set. The influence of these parameter were studied for NB layers NB1, NB5 and NB10 concentrating on the following features of the Ca^{2+} wave: peak amplitude, time to peak, Ca^{2+} wave width at half maximum, and Ca^{2+} concentration at the end of the Ca^{2+} wave (at 90 seconds' time point).

Model prediction of drug effect: suramin

With the model, we investigated the mechanism by which suramin influences the Ca^{2+} waves in ARPE-19 cells. First, we compared the peak amplitude, time to peak, Ca^{2+} wave width at half maximum, and Ca^{2+} concentration in the end of the Ca^{2+} wave at 90 seconds' time point between two experimental data sets: GA-treated and GA-suramin-treated data sets. Second, we made sensitivity analysis about the behaviour of P_2Y_2 receptor regulation parameters (K_1 , K_2 , k_r , k_p , k_e , ξ), since suramin is a known unspecific antagonist of P_2 receptors. Suramin has also been suggested to disrupt the coupling between the receptor in the cell membrane and the G-protein by blocking the association of the G-protein α and $\beta\gamma$ subunits [33]. Hence, the G-protein cascade parameters k_a , k_d and δ were also evaluated. The sensitivity analysis was done in the model for GA-treated data set (including model components I-V) in NB1, NB5 and NB10 layers. The parameter values were changed in the model by -25% and +25% in order to compare the effects of parameter modifications to the observed differences in the experimental data between GA-treated and GA-suramin-treated data sets. All other parameters were kept unchanged. Third, based on the results of this approach, the model was fitted to the GA-suramin-treated data set by refitting those P_2Y_2 receptor and G-protein cascade parameters that were observed to change the Ca^{2+} curve similarly to the differences seen in the experimental data between GA-treated and GA-suramin-treated data sets. This was done with Matlab SimBiology Parameter Fit task for each NB layer.

Detailed model equations

Time dependent changes in intracellular Ca^{2+} concentration $[\text{Ca}^{2+}]_i$ are presented in the model as a combination of Ca^{2+} fluxes

$$\frac{d[\text{Ca}^{2+}]_i}{dt} = J_{\text{SSCC}} + J_{\text{IP}_3\text{R}_3} + J_{\text{RyR}} - J_{\text{Pump}} + J_{\text{Leak}} + J_{\text{GJ,Ca}^{2+}}, \quad (6)$$

where the subscripts indicate the source of the flux: stretch-sensitive Ca^{2+} channels (J_{SSCC}), inositol 1,4,5-trisphosphate (IP_3) receptor type 3 ($J_{\text{IP}_3\text{R}_3}$), and ryanodine receptor (J_{RyR}). J_{Pump} combines the Ca^{2+} pumping functions of sarco/endoplasmic reticulum ATPase (SERCA) and the plasma membrane Ca^{2+} ATPase (PMCA). Leak Ca^{2+} current (J_{Leak}) describes the total leakage from the extracellular space and the endoplasmic reticulum (ER) to the cytoplasm. $J_{\text{GJ,Ca}^{2+}}$ is the Ca^{2+} flux through gap junctions.

I Stretch-sensitive Ca^{2+} channels (SSCCs). Stretch-sensitive Ca^{2+} channels (SSCCs) on the cell membrane are activated, when exposed to mechanical stimulation. Their closure is caused either by relaxation in the mechanical force or by their adaption to that mechanical force[34]. The SSCC model is described with Eqs 7–9. In this study, a model for SSCCs was developed according to the kinetic diagram shown in Fig 3, where C_{SSCC} describes the proportion of the channels in the closed state. O_{SSCC} is the proportion of SSCCs in the open state defined as

$$\frac{dO_{\text{SSCC}}}{dt} = \theta k_f - (\theta k_f + k_b) O_{\text{SSCC}}, \quad (7)$$

where k_f is the forward rate constant and k_b is the backward rate constant. Ca^{2+} flux via SSCCs (J_{SSCC}) is expressed as

$$J_{\text{SSCC}} = k_{\text{SSCC}} O_{\text{SSCC}}, \quad (8)$$

where k_{SSCC} is the maximum Ca^{2+} flux rate via SSCCs. Parameter θ is dimensionless, and describes the quantity of stretch induced at the time of mechanical stimulation, which then decreases with time

$$\frac{d\theta}{dt} = -k_\theta \theta, \quad (9)$$

according to a stretch-relaxation parameter k_θ .

II Purinergic receptor P_2Y_2 . The agonist-induced activation of the second messenger system, here P_2Y_2 , is represented by Eqs 10–16[21].The kinetic diagram for the P_2Y_2 receptor is presented in Fig 3. Some of the ligand-bound P_2Y_2 receptors on the cell surface are phosphorylated irreversibly at rate k_p , which causes desensitization of the receptors. Phosphorylated receptors are internalized at a rate k_e , and these internalized receptors are then dephosphorylated and recycled back to the surface at rate k_r . G-proteins can only be activated by the unphosphorylated P_2Y_2 receptors [R^S] defined by

$$\frac{d[R^S]}{dt} = k_r[R_T] - \left(k_r + \frac{k_p[L]}{K_1 + [L]} \right) [R^S] - k_r[R_p^S], \quad (10)$$

where $[R_T]$ denotes the total number of surface receptors, K_1 is the dissociation constant for unphosphorylated receptors, and $[L]$ is the extracellular ligand concentration. The total

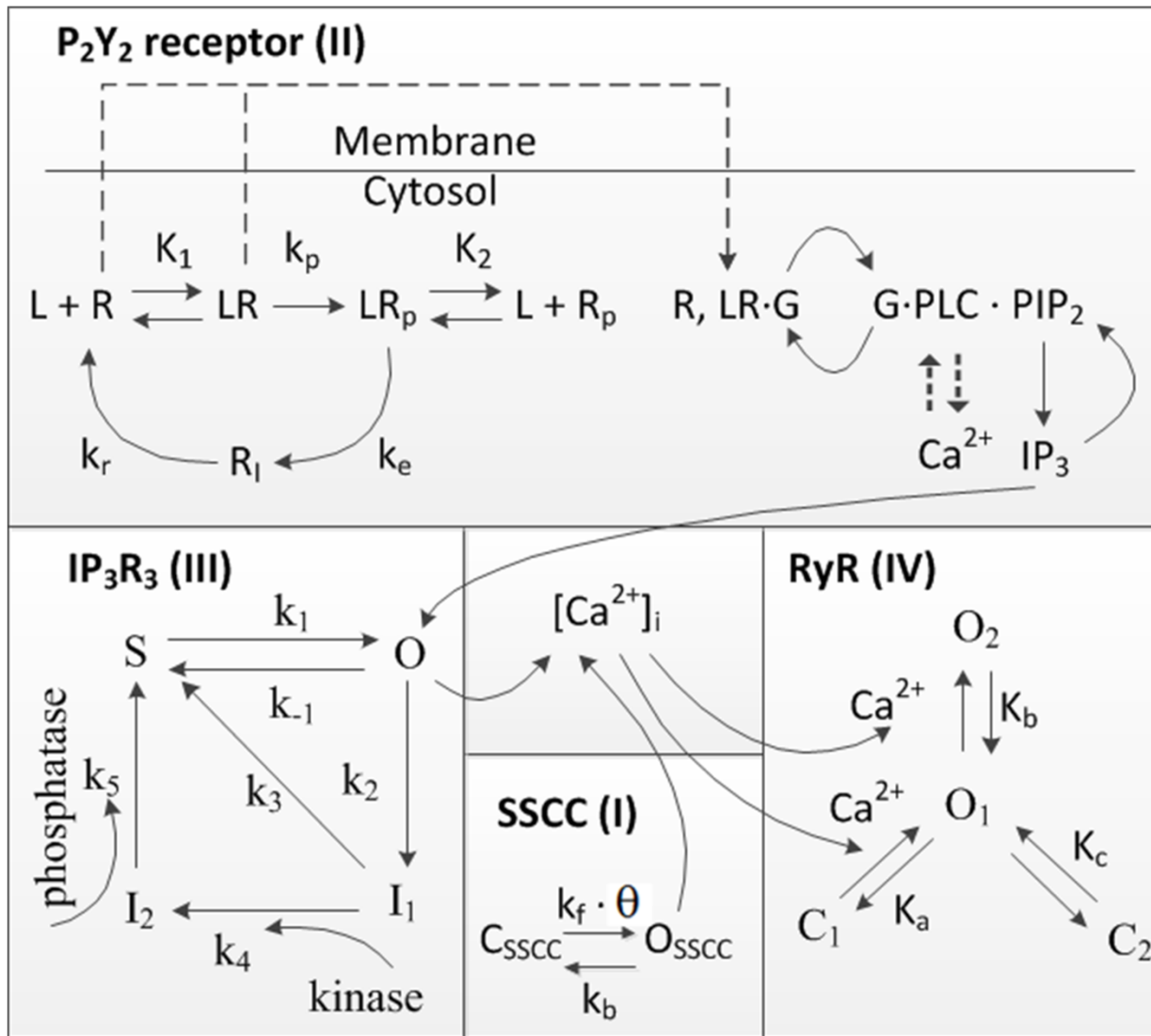


Fig 3. Kinetic diagram. Kinetics of the model component I (SSCC) were combined with the kinetics of model components II–IV from the original models of the P₂Y₂ receptor[21], IP₃R₃[22], and RyR[23].

doi:10.1371/journal.pone.0128434.g003

number of phosphorylated surface receptors [R_p^S] is

$$\frac{d[R_p^S]}{dt} = [L] \left(\frac{k_p[R^S]}{K_1 + [L]} - \frac{k_e[R_p^S]}{K_2 + [L]} \right), \quad (11)$$

where K₂ is the dissociation constant for phosphorylated receptors. The binding of the ligand to the G-protein coupled receptor P₂Y₂ results in a cascade of events leading to the activation of enzyme phospholipase C (PLC). This enzyme then hydrolyses the phosphatidylinositol 4,5-bisphosphate (PIP₂) to IP₃. The activation rate (k_a) of the G-protein is proportional to two ratios: the ratio of the activities of the ligand unbound and bound receptor species (δ), and the ratio of the number of ligand bound receptors and the total number of receptors (p_r). Denoting the deactivation of G-protein to occur at a deactivation rate of k_d, the equations for the amount

of $G\alpha \cdot GTP$ labeled as $[G]$ as well as for the ratio p_r can be expressed as

$$\frac{d[G]}{dt} = k_a(\delta + p_r)([G_T] - [G]) - k_d[G], \quad (12)$$

and

$$p_r = \frac{[L][R^S]}{\xi[R_T](K_1 + [L])}. \quad (13)$$

Equation for the concentration of IP_3 is

$$\frac{d[IP_3]}{dt} = r_h N_a^{-1} v^{-1} [PIP_2] - k_{deg}[IP_3] + J_{GJ,IP_3}, \quad (14)$$

where k_{deg} is the degradation rate of IP_3 and J_{GJ,IP_3} is the IP_3 flux through gap junctions. The rate coefficient for PIP_2 hydrolysis (r_h) includes the effective signal gain parameter (α) and the dissociation constant for Ca^{2+} binding to PLC (K_3) that can be expressed as

$$r_h = \alpha \left(\frac{[Ca^{2+}]_i}{K_3 + [Ca^{2+}]_i} \right) [G]. \quad (15)$$

Replenishment of PIP_2 is required for IP_3 production to be maintained over sustained periods of agonist stimulation. The equation for the number of PIP_2 molecules $[PIP_2]$ is

$$\frac{d[PIP_2]}{dt} = -(r_h + r_r)[PIP_2] - r_r N_a v [IP_3] + r_r [(PIP_2)_T], \quad (16)$$

where r_r represents the PIP_2 replenishment rate and $[(PIP_2)_T]$ the total number of PIP_2 molecules.[21]

III IP_3 receptor type 3 (IP_3R_3). The IP_3 receptor type 3 (IP_3R_3) function is represented by the Eqs 17–21[22]. The kinetic diagram for IP_3R_3 is shown in Fig 3. The IP_3 -induced release of Ca^{2+} from the ER through IP_3R_3 ($J_{IP_3R_3}$) is

$$J_{IP_3R_3} = k_{IP_3R_3} O^4, \quad (17)$$

where $k_{IP_3R_3}$ is the maximum rate of Ca^{2+} release, and IP_3R_3 comprises four subunits that all must be in the open state (O) for the receptor to conduct. The steady-state proportion of open receptors (O) is

$$O = \frac{\phi [IP_3]}{\frac{k_{-1} + k_2}{k_1} \phi + [IP_3]}, \quad (18)$$

Where ϕ function controls the sensitivity of IP_3R_3 to $[IP_3]$, and it can be expressed as

$$\phi = \frac{1}{1 + \frac{k_2}{k_3 + k_4} \left(1 + \frac{k_4}{k_5} \right)}, \quad (19)$$

with rate coefficients k_{-1} , k_2 , k_3 , and k_5 being constants. Coefficient k_1 describes a rate for IP_3R_3 transition from shut state (S) to open state (O)

$$k_1 = \frac{\alpha_1 [Ca^{2+}]_i^3}{\beta_1^3 + [Ca^{2+}]_i^3}, \quad (20)$$

where constant α_1 is the maximum rate of S to O transition, and β_1 is the $[Ca^{2+}]_i$ at which the rate is half of its maximum. Coefficient k_4 expresses the rate for IP_3R_3 from the first inactivated

state (I_1) to the second inactivated state (I_2). It can be expressed as

$$k_4 = \frac{\alpha_4 [IP_3]}{\beta_4 + [IP_3]}, \quad (21)$$

where the I_1 to I_2 transition is agonist specific and involves a phosphorylation of IP_3R_3 by kinase activity. This is defined by parameter α_4 that denotes the maximum rate of I_1 to I_2 transition, while β_4 denotes the value of $[IP_3]$ at which the rate is half maximal.[22]

IV Ryanodine receptor (RyR). The ryanodine receptor (RyR) dynamics were modeled by Keizer & Levine 1996[23] with Eqs 22–24. In Fig 3 the kinetic diagram for RyR is illustrated. The Ca^{2+} release from the ER through RyR (J_{RyR}) is defined by the maximum RyR flux rate (k_{RyR}) multiplied by the open probability (P_{RyR}) as

$$J_{RyR} = k_{RyR} P_{RyR} \quad (22)$$

where

$$P_{RyR} = \left(\frac{w^\infty \left(1 + \left(\frac{[Ca^{2+}]_i}{K_b} \right)^3 \right)}{1 + \left(\frac{K_a}{[Ca^{2+}]_i} \right)^4 + \left(\frac{[Ca^{2+}]_i}{K_b} \right)^3} \right), \quad (23)$$

and where w^∞ is the RyR sensitivity function

$$w^\infty = \left(\frac{1 + \left(\frac{K_a}{[Ca^{2+}]_i} \right)^4 + \left(\frac{[Ca^{2+}]_i}{K_b} \right)^3}{1 + \frac{1}{K_c} + \left(\frac{K_a}{[Ca^{2+}]_i} \right)^4 + \left(\frac{[Ca^{2+}]_i}{K_b} \right)^3} \right), \quad (24)$$

and K_a , K_b , and K_c are dissociation constants. [23]

V Sarco/endoplasmic reticulum Ca^{2+} ATPase (SERCA) and plasma membrane Ca^{2+} ATPase (PMCA). J_{Pump} combines the pumping functions of sarco/endoplasmic reticulum Ca^{2+} ATPase (SERCA) and plasma membrane Ca^{2+} ATPase (PMCA)

$$J_{Pump} = \frac{V_{Pump} [Ca^{2+}]_i^2}{K_{Pump}^2 + [Ca^{2+}]_i^2}, \quad (25)$$

where V_{Pump} indicates the maximum flux rate of the pumps and K_{Pump} states the $[Ca^{2+}]_i$ for half-maximal pumping rate.

VI Gap junctions (GJs). Gap junctions (GJs) and the Ca^{2+} flux via GJs ($J_{GJ,Ca^{2+}}$) are modeled as

$$J_{GJ,Ca^{2+}} = \frac{D_{Ca^{2+}}}{A_{n-1,n}} ([Ca^{2+}]_{i-1} - [Ca^{2+}]_i) - \frac{D_{Ca^{2+}}}{A_{n,n+1}} ([Ca^{2+}]_i - [Ca^{2+}]_{i+1}), \quad (26)$$

where n is the number of the NB layer. The NB layer n receives Ca^{2+} from the previous NB layer $n - 1$ and delivers Ca^{2+} to the next NB layer $n + 1$ according to the concentration gradient. Similarly, IP_3 flux through GJs (J_{GJ,IP_3}) is modelled as

$$J_{GJ,IP_3} = \frac{D_{IP_3}}{A_{n-1,n}} ([IP_3]_{i-1} - [IP_3]_i) - \frac{D_{IP_3}}{A_{n,n+1}} ([IP_3]_i - [IP_3]_{i+1}), \quad (27)$$

where n is the number of the NB layer. $D_{Ca^{2+}}$ is the diffusion coefficient for Ca^{2+} and D_{IP_3} is the diffusion coefficient for IP_3 . These diffusion coefficients do not take into account the open probability, regulation, or density of the GJs as they describe the actual movement of Ca^{2+} and

IP_3 from one NB layer to the next NB layer. As an exception to other NB layers, the fluxes from MS cell to NB₁ layer are modelled by parameters $In_{Ca^{2+}}$ and In_{IP_3} for Ca^{2+} and IP_3 , respectively. Similarly, the fluxes from NB₁₀ layer to distant cell layers are modelled with parameters $Out_{Ca^{2+}}$ and Out_{IP_3} .

Parameter A describes the area of the cell membranes connecting the neighbouring NB layers in the monolayer. The value for A is received by multiplying the area of one hexagon side, that is the length of the hexagon side ($l = 7\mu m$) times the height of the cell ($h = 12\mu m$), by the number of hexagon edges between the two NB layers as

$$A_{n \rightarrow n+1} = ((3 + 2(n - 1))6)lh, \quad (28)$$

where n is the number of the NB layer ($n = 1, 2, 3 \dots 10$). Each NB layer has six cells with three connecting sides and $(n-1)6$ cells with two connecting sides (see Fig 1). In other words, the area (A) increases with distance from the central MS cell.

Results

Polarization of the ARPE-19 monolayer

Polarization of the ARPE-19 monolayer was demonstrated by immunolabeling the tight junctions in the monolayer. Confocal microscopy image (Fig 4) shows that within 2 days the ARPE-19 cells have formed a monolayer where ZO-1 is localised continuously in the junctions of the cells, forming a homogeneous network. This can be taken as an indication of the polarization of the epithelial cell culture [35].

Ca^{2+} signal propagation mechanisms

The fittings of the model to the experimental data in the NB1-NB10 layers are illustrated in Fig 5A for the GA-treated data set and in Fig 5B for the control data set. The model simulations managed to catch very well the features of the experimental data in both data sets. In GA-treated data set (Fig 5A), the simulations closely followed the data in peak amplitude, time to peak, Ca^{2+} wave width at half maximum and end Ca^{2+} concentration in NB1-NB9 layers. In NB10 layer, however, time to peak was longer in the simulation results than in the data. In the control data set (Fig 5B), the Ca^{2+} wave features differed slightly between the model and the data, but overall the curve shape of the model followed the data reasonably well. R^2 values describing the goodness of fit are presented in Table 4. In GA-treated data set and control data set R^2 values were higher than 0.8 in NB1-NB9 and lower than 0.8 in NB10. Hence, 90% of the fits in GA-treated data set and control data set resulted in $R^2 > 0.8$.

The model includes the model components of SSCCs, P₂Y₂ receptors, IP₃R₃s, RyRs, Ca^{2+} pumps and GJs, and the parameters were either obtained from previous studies or defined in this study for ARPE-19. The basic fit was done in GA-treated data set for NB5, but the SSCC model component was fitted in NB1 (Table 2). Three location-specific parameters were defined in this study: stretch (θ), extracellular ligand concentration (L) and phosphorylation rate of IP₃R₃ (α_4) (Table 3). The stretch (θ) and extracellular ligand concentration (L) decayed exponentially from NB1 towards the distant NB cell layers. The IP₃R₃ phosphorylation rate regulated by the kinase activity (α_4) increased following a shallow exponential, almost linear function, from NB1 to NB10. The corresponding values of α_4 with the distance were lower in the control data set (Eq 5) than in the GA-treated data set (Eq 4) indicating a possible role of IP₃ receptor phosphorylation rate as a regulator of Ca^{2+} signaling. The GJ model component was parameterized in control data set for NB1. GJs mediated the Ca^{2+} signal by allowing the diffusion of Ca^{2+} and IP_3 between adjacent cell layers so that the fluxes of these species decreased with

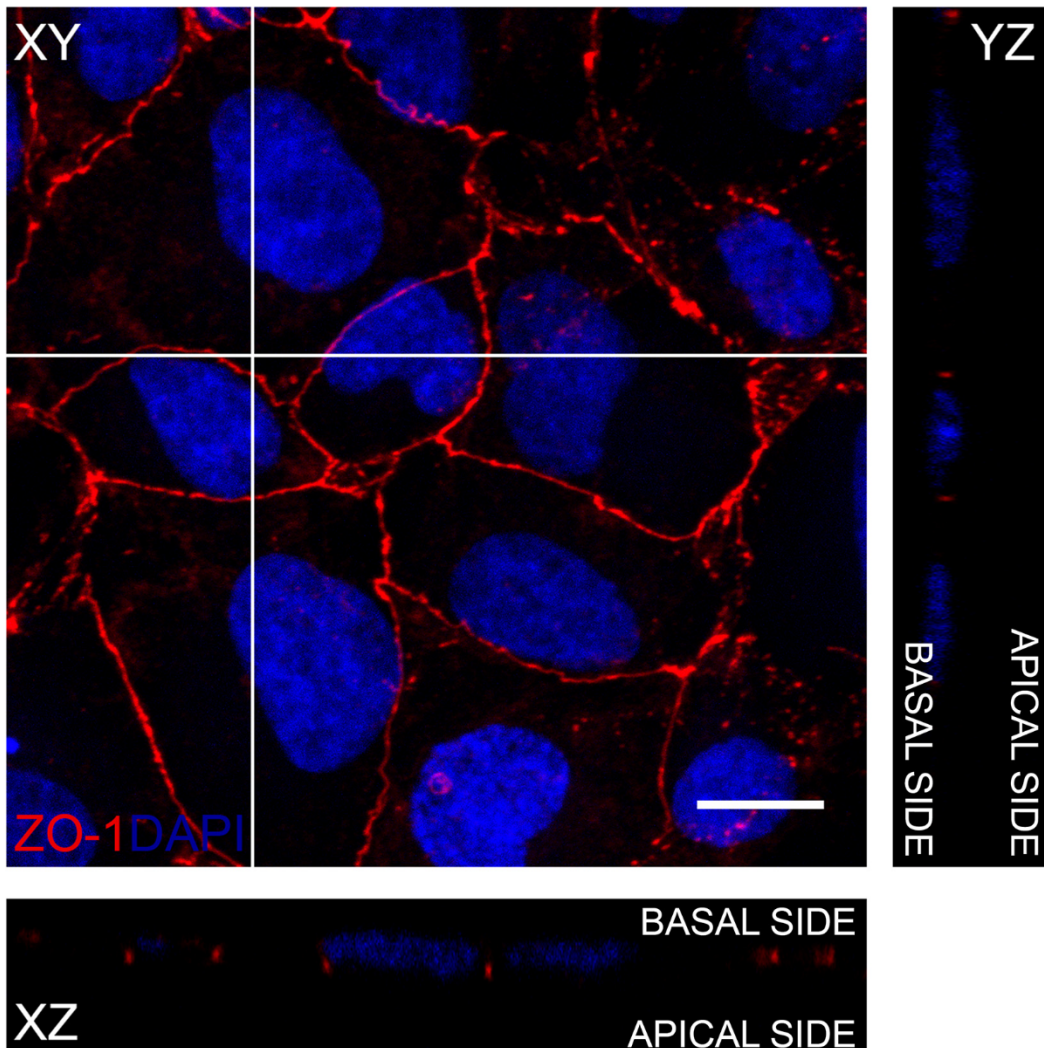


Fig 4. Polarization of the ARPE-19 monolayer. Z-projections (XZ and YZ) from apical side to basal side and maximum intensity projection of the XY plane in the ARPE-19 monolayer represent the localization of Zonula Occludens (ZO-1, red) in the confocal micrograph after immunofluorescence labeling with the nuclear label 4',6-diamidino-2-phenylindole (DAPI, blue). Scale bar is 10 μ m.

doi:10.1371/journal.pone.0128434.g004

distance from the MS cell due to the increasing area of the cell membranes connecting the NB layers (Table 3).

The resulting model of mechanical stimulus induced Ca^{2+} dynamics is: 1) Cells near the stimulus site conduct Ca^{2+} through plasma membrane SSCCs, and gap junctions conduct the Ca^{2+} and IP_3 between cells further away from stimulated cell. 2) The MS cell secretes one or several types of ligand to the extracellular space where the ligand diffusion mediates the Ca^{2+} signal so that the ligand concentration decreases with distance. 3) The phosphorylation of the IP_3 receptor defines the cell's sensitivity to the extracellular ligand attenuating the Ca^{2+} signal in the distance.

Results of the sensitivity analysis

The sensitivity of the four Ca^{2+} wave features described in Materials and Methods was studied for a set of parameters that were fitted in this study for NB1, NB5 and NB10 layers (Fig 6).

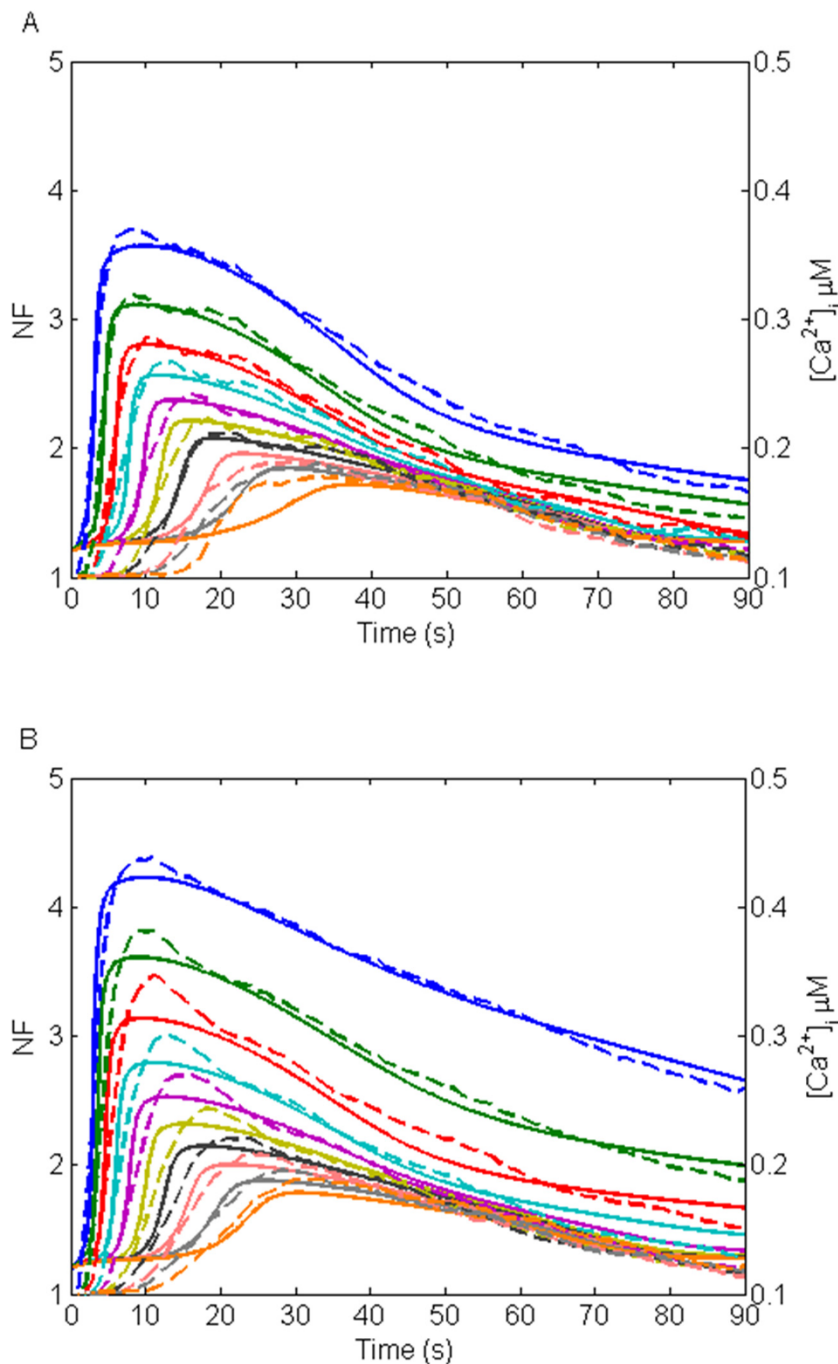


Fig 5. Fittings of the model to the experimental data. (A) GA-treated, and (B) control data sets with dashed lines representing the data in dimensionless NF units and solid lines representing the model simulations with arbitrary units representing $[Ca^{2+}]_i$ in μM concentrations. The uppermost curve pair (blue) represents NB1, the second uppermost NB2 (green), followed by NB3 (red), NB4 (light blue), NB5 (purple), NB6 (yellow), NB7 (black), NB8 (light red), NB9 (grey), and NB10 (orange).

doi:10.1371/journal.pone.0128434.g005

From the location-dependent parameters, θ , L and α_4 , Ca^{2+} wave features were most sensitive to modifications in α_4 and the least sensitive to modifications in θ . Overall, decreasing the stretch parameter (θ) resulted in faster Ca^{2+} waves in NB1 (Fig 6B). Increasing the extracellular

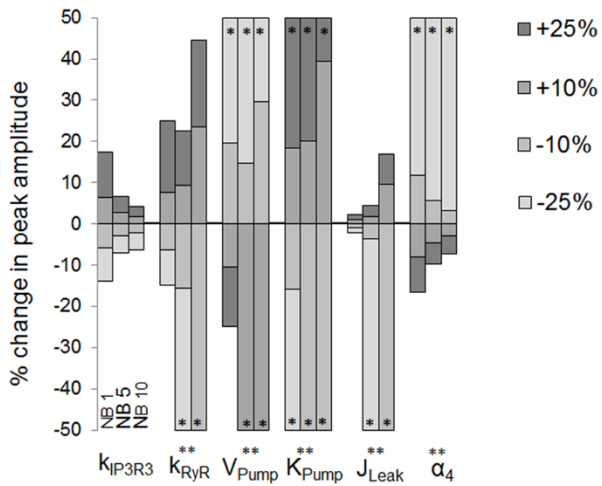
Table 4. R^2 values indicating the goodness of fit between the model and the data.

Data set	NB1	NB2	NB3	NB4	NB5	NB6	NB7	NB8	NB9	NB10
GA-treated	0.9839	0.9815	0.9811	0.9651	0.9716	0.9627	0.9677	0.9326	0.8837	0.4561
Control	0.9665	0.9613	0.9454	0.9653	0.9686	0.9558	0.9508	0.9419	0.9108	0.6259
GA-suramin-treated	0.8633	0.8543	0.9344	0.9323	0.9414	0.9156	0.9253	0.7812	0.6110	0.2297

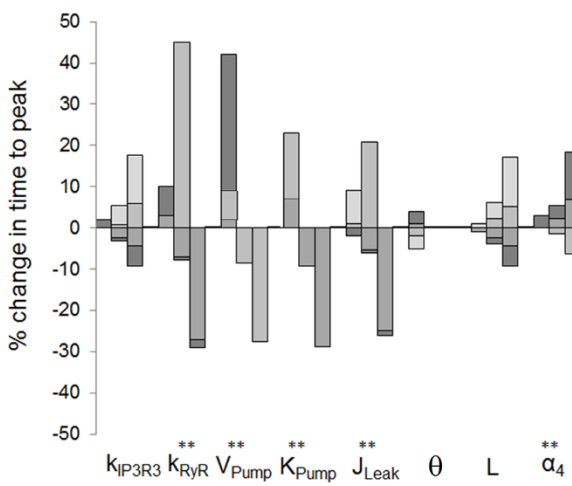
R^2 values are listed separately for each data set and NB layer.

doi:10.1371/journal.pone.0128434.t004

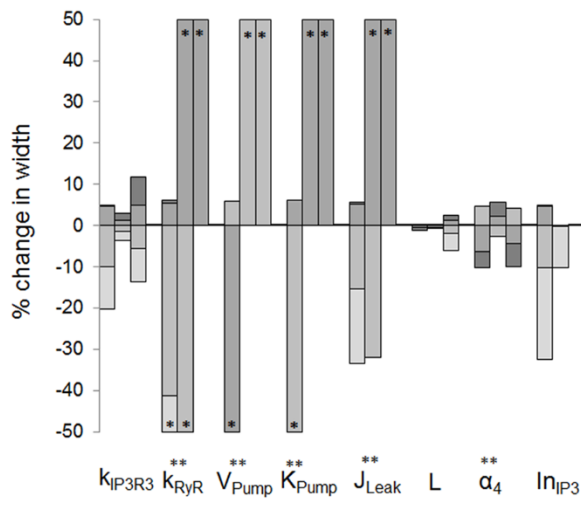
A



B



C



D

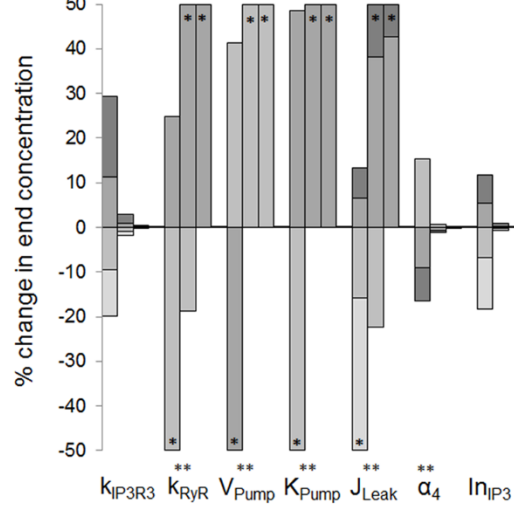


Fig 6. Sensitivity analysis of the model parameters. Percentage changes in Ca^{2+} wave (A) peak amplitude, (B) time to peak, (C) Ca^{2+} wave width at half maximum, and (D) end Ca^{2+} concentration at 90 seconds' time point due to changes in model parameters k_{IP3R3} , k_{RyR} , V_{Pump} , K_{Pump} , J_{Leak} , θ , L , α_4 , In_{IP3} , $In_{Ca^{2+}}$, D_{IP3} , and $D_{Ca^{2+}}$ as marked in the x-axis. The analysis was carried out in NB layers NB1, NB5 and NB10 as denoted in (A) for parameter k_{IP3R3} . The amount of modification (-25%, -10%, +10% or +25%) is shown in the grayscale of the histogram. The histogram bar is marked with asterisk (*) if the change was greater than 50%, and with double asterisk (**) if parameter modification did not result typical Ca^{2+} waveform. Regarding each Ca^{2+} wave feature, the parameter is illustrated only if the change was more than 5%.

doi:10.1371/journal.pone.0128434.g006

ligand concentration (L) in turn decreased the time to peak (Fig 6B) and increased the Ca^{2+} wave width at half maximum (Fig 6C). The effects of the changes in IP_3 receptor phosphorylation rate (α_4) on Ca^{2+} wave features were complex: with decreasing α_4 Ca^{2+} wave peak amplitude increased (Fig 6A), time to peak decreased (Fig 6B), the Ca^{2+} wave width at half maximum increased or decreased depending on the NB layer (Fig 6C), and the end concentration increased (Fig 6D). The Ca^{2+} wave features were insensitive to gap junction related parameters $In_{\text{Ca}^{2+}}$, D_{IP_3} and $D_{\text{Ca}^{2+}}$ so that the tested modifications in their values resulted in less than 5% change in the features from the original conditions. Thus, they are not illustrated in Fig 6. However, increasing IP_3 input to NB1 via GJs (In_{IP_3}) increased the Ca^{2+} wave width at half maximum (Fig 6C) and end concentration (Fig 6D), and the sensitivity was significantly higher in NB1 layer than in the more distant NB layers. In general, the sensitivity of the model to the changes in tested parameters depended on the NB layer and thus on the distance to the MS cell. Few parameters, however, were independent of the location (parameters $k_{\text{IP}_3 R_3}$, k_{RyR} , V_{Pump} , K_{Pump} , J_{Leak}), but changes in their values affected significantly the investigated Ca^{2+} wave features.

Possible suramin effect on attenuation of Ca^{2+} waves

Similarly to the general sensitivity analysis, the four Ca^{2+} wave features were compared between the experimental GA-treated and GA-suramin-treated data sets as well in NB1, NB5 and NB10 layers (Fig 7A). In the GA-suramin-treated data set, differences in peak amplitude were less than 10% compared to the GA-treated data set. However, time to peak decreased for NB1 and increased for NB5 and NB10 layers in the GA-suramin-treated data set. Furthermore, in this data set the Ca^{2+} wave width at half maximum and the end Ca^{2+} concentration were lower than in the GA-treated data set.

Since suramin is a known P_2 receptor blocker, we studied the sensitivity of the model to P_2Y_2 receptor parameters for the GA-treated data set (including model components I-V) by changing their values by $\pm 25\%$. Similarly, G-protein cascade parameters were studied as well to consider the possible effect of suramin to disrupt the coupling between the receptor in the cell membrane and the G-protein. Our aim was to investigate the degree to which the observed differences in the Ca^{2+} wave features between GA-treated and GA-suramin-treated data sets could be accounted for by the changes in these parameters. The sensitivity analysis revealed that the modifications in P_2Y_2 unphosphorylated receptor dissociation constant (K_1) and P_2Y_2 receptor phosphorylation rate (k_p) indeed induced changes that were similar to the experimental observations (see Fig 7A): increase in K_1 modified the time to peak (Fig 7B) and increase in k_p narrowed the Ca^{2+} wave width at half maximum (Fig 7C). This would indicate disrupted ligand binding to the receptor or a higher phosphorylation rate of P_2Y_2 receptors as well as a faster desensitization of the receptors after ligand binding. P_2Y_2 receptor parameters K_2 , k_r , k_e , ξ , on the contrary, had a negligible influence on Ca^{2+} wave behaviour: the modifications of these parameters by $\pm 25\%$ resulted only in less than 3% change on Ca^{2+} wave features, as was the case also for G-protein cascade parameter δ . G-protein cascade parameters G-protein activation rate (k_a) (Fig 7D) and G-protein deactivation rate (k_d) (Fig 7E) had diverse effects on the Ca^{2+} wave features: for example decreasing k_a and increasing k_d narrowed the Ca^{2+} wave width at half maximum in NB1 and NB5, but widened it in NB10. Thus, their behaviour did not follow the observations from the experimental data and therefore these factors were not considered to be responsible for the effects of suramin on the Ca^{2+} wave.

Fig 7F illustrates the fit of the model to the GA-suramin-treated data set after refitting the model parameters K_1 and k_p . The values of these parameters ranged as follows: K_1 values decreased from $8.83\mu\text{M}$ in NB1 to $5.15\mu\text{M}$ in NB10 and k_p values decreased from 0.19s^{-1} in NB1

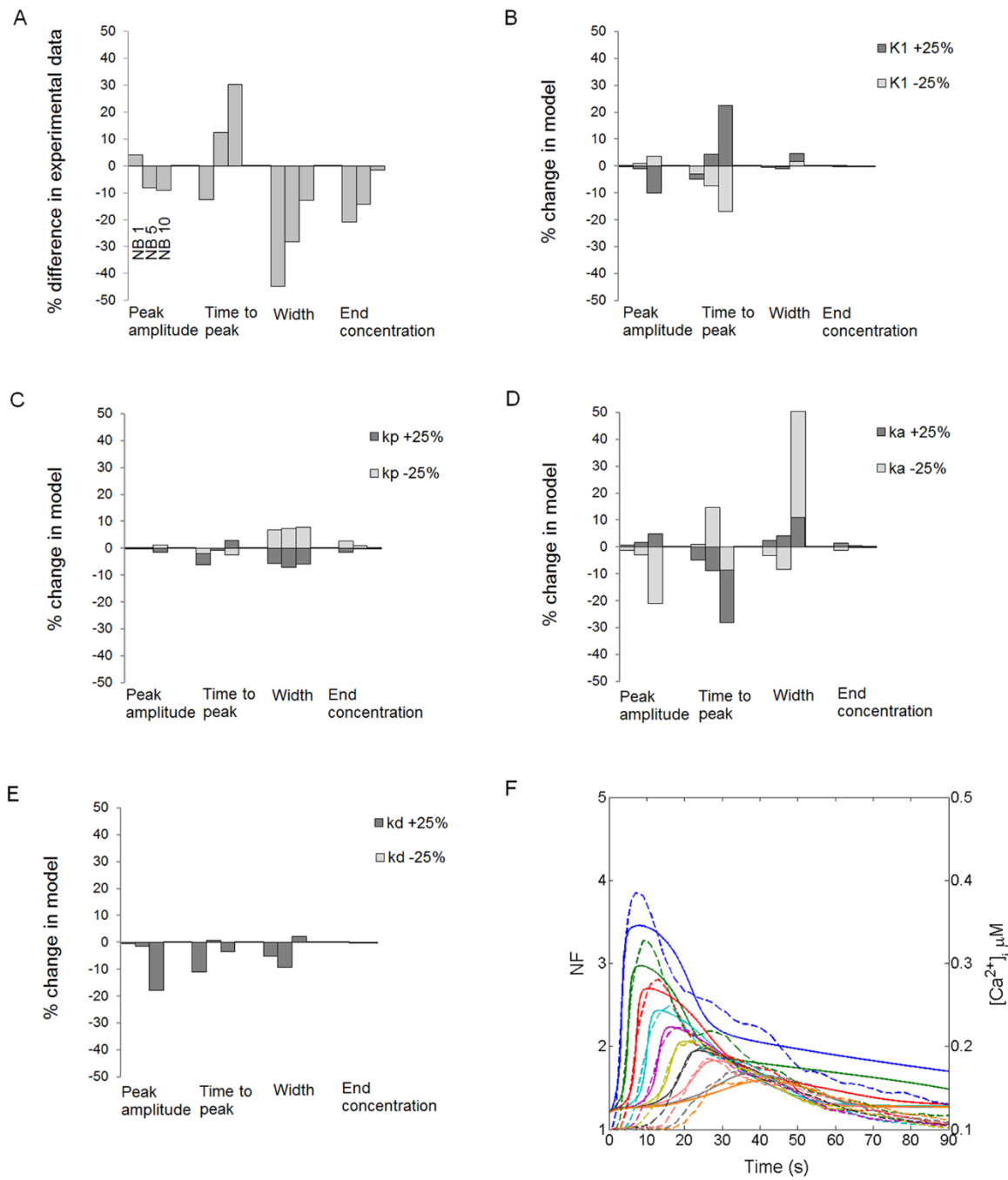


Fig 7. Suramin effects on Ca²⁺ wave. (A) Comparison of the peak amplitude, time to peak, Ca²⁺ wave width at half maximum, and end Ca²⁺ concentration at 90 seconds' time point in cell layers NB1, NB5 and NB10 between the experimental GA-treated and GA-suramin-treated data sets. The deviations of each Ca²⁺ wave feature in GA-suramin-treated data set from GA-treated data set are expressed as percentages. (B) Unphosphorylated P₂Y₂ receptor dissociation constant (K₁), (C) P₂Y₂ receptor phosphorylation rate (k_p), (D) G-protein activation rate (k_a), and (E) G-protein deactivation rate (k_d) were changed in the model for GA-treated data set either -25% or +25%, as denoted in the grayscale of the histogram, and the percentage change in each Ca²⁺ wave feature is illustrated. (F) Fitting of the model to the GA-suramin-treated data set. Dashed lines represent the data in dimensionless NF units, whereas solid lines represent the model simulations with arbitrary units representing [Ca²⁺]_i in μM concentrations. The uppermost curve pair (blue) represents NB1, the second uppermost NB2 (green), followed by NB3 (red), NB4 (light blue), NB5 (purple), NB6 (yellow), NB7 (black), NB8 (light red), NB9 (grey), and NB10 (orange).

doi:10.1371/journal.pone.0128434.g007

to 0.05s^{-1} in NB10. Overall, the values of K_1 and k_p were higher in the GA-suramin-treated data set than in the GA-treated data set. The simulated curves seem to fit well to the experimental data, except in NB1 layer at the end of the Ca^{2+} wave. In GA-suramin-treated data set, R^2 values were higher than 0.8 in NB1-NB7 and lower than 0.8 in NB8-NB10 (Table 4). 70% of the fits in GA-suramin-treated data set resulted in $R^2 > 0.8$ indicating that the model explains only partially the combined effect of GA and suramin on Ca^{2+} waves especially in the distant NB layers.

Discussion

The ARPE-19 cell line is an important biological model of human RPE despite its certain limitations [20]. This paper presents the first computational RPE model of Ca^{2+} signaling using the experimental data measured from the ARPE-19 monolayer after mechanical stimulation. We aimed to create a model that combines the most important Ca^{2+} signaling mechanisms in ARPE-19 cells so that the model can be used later in the development of more complicated RPE and epithelial models. Furthermore, the model was used to simulate and explain the Ca^{2+} signaling of epithelia, especially RPE, taking into account the following factors: 1) cells are on the monolayer; 2) they are connected to each other by GJs permeating Ca^{2+} and IP_3 , and 3) the cells are most probably experiencing different stretching and chemical conditions depending on their distance from the mechanical stimulation site. To the best of our knowledge, this is the first time as Ca^{2+} signaling model has been implemented for the ARPE-19 monolayer. The model uses a set of location specific parameters including stretch, extracellular ligand concentration, and IP_3R_3 phosphorylation rate as well as the Ca^{2+} and IP_3 fluxes through GJs.

The identity of the extracellular ligand

The airway epithelium secretes the signal carriers ATP or UTP to the extracellular space in response to mechanical stimulation [16,36]. The connection of these ligands to Ca^{2+} signaling as extracellular signal mediators has been mathematically modeled [16]. It is likely that a similar function can be linked to ARPE-19 or RPE, where the ligand interacts with the cell membrane P_2Y_2 receptors. In our model, the ligand carried the signal in the extracellular space from the MS cell towards the distant NB cell layers after mechanical stimulation. According to our model, the extracellular ligand concentration decreased exponentially from NB1 towards NB10. We suggest, based on our modeling results, that the MS cell secretes ligand to the extracellular space. Epithelial cells such as ARPE-19 have been shown to secrete ATP under different stimuli [37,38]. On the other hand, the ligand degradation by ectonucleotidase activity [39] decrease the ligand concentration. The model predicts that the magnitude of the extracellular ligand concentration partly defines the nature of the cell response: higher and faster Ca^{2+} waves were observed with higher ligand concentrations. The ligand concentration was derived from diffusion equation, and the obtained exponential decay function fitted well to the experimental data. Experimental studies show that the Ca^{2+} wave peak amplitude value increases with increased ligand concentration in cultured human RPE [30] and in human airway epithelium [6]. Also, in the mathematical model of Warren et al. 2010 [16], it was observed that the time to peak for human airway epithelium decreased as the ligand concentration increased. These observations are in good agreement with our model.

The role of IP_3 receptor phosphorylation rate

The phosphorylation of the IP_3 receptor represents an important regulatory mechanism for Ca^{2+} release [40–42]. It has been shown that the production of cyclic AMP (cAMP) through the

activation of the adenylyl cyclase pathway leads to the activation of protein kinase A that phosphorylates IP₃ receptors[43].

Our simulation results show that the maximal phosphorylation rate of IP₃R₃ (α_4) followed a shallow exponential, almost linear, increase from NB1 to NB10 in all three data sets. The parameter α_4 has previously been modeled as agonist specific only [22]. It is of note, however, that in addition to ATP or UTP and their interaction with P₂Y₂ receptors, also other types of ligand-receptor interactions may occur. One plausible explanation could be that MS cell secretes different types of ligands, because its cell membrane was broken in mechanical stimulation. This would further lead to complex biological interactions at the cellular level, which is seen as a chance of this parameter with cell location.

The need to model α_4 separately for the GA-treated data set and the control data set may be related to the functioning of the GJs, especially to their ability to alter ligand secretion in different cell types. Previous studies show that GJs participate in the regulation of the release of signaling molecules to the extracellular medium [44]. In astrocytes, as an example, GJs have been proposed to regulate the release of glutamate[45], an excitatory neurotransmitter and an important regulator of astrocyte Ca²⁺ oscillations[46].

Overall, α_4 parameter may reflect a number of ligands and cell mechanisms not modelled in this nor other epithelial Ca²⁺ models. The low α_4 values near the MS cell enable higher and faster Ca²⁺ waves at corresponding ligand concentrations compared to the distal cell layers, where higher levels of kinase activity attenuate and slow down the signal. This aligns well with the literature. In RPE, the addition of 8-Br-cAMP counteracted the elevation of [Ca²⁺]_i induced by connective tissue growth factor (CTGF)[47], and the cell migration inhibitor adrenomedullin increased intracellular cAMP and decreased [Ca²⁺]_i[48]. The effect of the adenylyl cyclase pathway on IP₃R kinetics has been ignored in most of the previously published Ca²⁺ models e.g.[16,21,29], possibly because the kinase activity may not have been activated in those cell types or experimental conditions.

Gap junctions in Ca²⁺ wave propagation

GJs connect the adjacent cells together and allow the diffusion of signaling molecules between them. The diffusion through GJs has previously been modeled, for example, in airway epithelium[16]. In our model, GJs carried the Ca²⁺ signaling molecules between the NB layers based on the Ca²⁺ and IP₃ concentration gradients, and permeated Ca²⁺ and IP₃ selectively. As expected, NB layers near the MS cell were more sensitive to IP₃ input than the distant NB layers, and this was seen especially in the end Ca²⁺ concentration at 90 seconds' time point.

Possible Ca²⁺ wave attenuation mechanisms of suramin

In the GA-suramin-treated data set, the experimental data was reproduced in our model by increasing the unphosphorylated receptor dissociation constant, which likely reflects disrupted ligand binding, and by increasing the phosphorylation rate of the P₂Y₂ receptors to enhance their desensitization. This may indicate that suramin targets on P₂Y₂ receptors as an unspecific P₂ receptor antagonist attenuating the Ca²⁺ wave. This intriguing model hypothesis driven from the model results needs to be confirmed experimentally. It is worth noting, however, that suramin has also been considered to disrupt the coupling between the receptor in the cell membrane and the G-protein by blocking the association of the G-protein α and $\beta\gamma$ subunits[33]. In our model, modifications in G-protein cascade parameters influenced the peak amplitude, time to peak and Ca²⁺ wave width at half maximum. Despite the observed diversity in their effects between the NB layers, it is possible that suramin targets the G-protein cascade as well, by acting as an attenuator of the Ca²⁺ wave.

Limitations of the model

Our work presents a computational model of epithelial Ca^{2+} signaling based on experimental work on the ARPE-19 cell line. This cell line is used extensively as a model of RPE, although it differs from it to some extent. The limitations of ARPE-19 compared to native human RPE arise, for example, from cell organization and metabolism[20]. Importantly for our study, ARPE-19 cell line in our experimental setup lacked pigmentation which resulted in a lack of the large Ca^{2+} stores, melanosomes, and needs to be taken into account when expanding our model to describe native RPE. In addition, we confirmed the polarity of the ARPE-19 monolayer with confocal microscopy. Trans-epithelial resistance (TER) that is a general measure of epithelial integrity was not measured due to technical challenges to perform the measurements on glass cover slips with our present equipment [49]. Nevertheless, the computational model created in this study describes the most important components of epithelial and ARPE-19 Ca^{2+} activity. Thus it provides a good basis to address the native RPE in the future, even though it, being based on an *in vitro* model of RPE, needs to be considered only as a model. To improve the model further, experimental data and model implementations on certain additional Ca^{2+} related mechanisms, such as P_2X receptors[50], voltage-sensitive Ca^{2+} channels[51] and $\text{Na}^+/\text{Ca}^{2+}$ exchangers[52] would be well warranted. Finally, it is worth noting that the experimental work of Abu Khamidakh et al. 2013[5] did not produce absolute Ca^{2+} concentrations, and therefore our model also features only relative Ca^{2+} activity.

Conclusions

A full mathematical understanding of RPE and epithelial Ca^{2+} signaling would allow one to simulate cellular Ca^{2+} responses under several physiological, pathological, and experimental conditions. Our present model represents significant progress towards this goal since it is able to reproduce the experimental data from an RPE type epithelium, ARPE-19 cell line, in different conditions, simulate several epithelial Ca^{2+} signaling mechanisms, and predict drug responses in the epithelia. Our future work will include further development of the model especially focusing on the role of the voltage sensitive Ca^{2+} channels in the RPE.

Author Contributions

Conceived and designed the experiments: IV AA KJ SN JH. Performed the experiments: IV AA. Analyzed the data: IV AA SN. Contributed reagents/materials/analysis tools: IV AA HS JH. Wrote the paper: IV AA MP HS KJ JH SN.

References

1. Sanderson MJ, Charles AC, Boitano S, Dirksen ER. Mechanisms and function of intercellular calcium signaling. *Mol Cell Endocrinol.* 1994; 98: 173–187. PMID: 8143927
2. Konari K, Sawada N, Zhong Y, Isomura H, Nakagawa T, Mori M. Development of the blood-retinal barrier in vitro: Formation of tight junctions as revealed by occludin and ZO-1 correlates with the barrier function of chick retinal pigment epithelial cells. *Exp Eye Res.* 1995; 61: 99–108. PMID: 7556475
3. Wimmers S, Karl MO, Strauss O. Ion channels in the RPE. *Prog Retin Eye Res.* 2007; 26: 263–301. PMID: 17258931
4. Himpens B, Stalmans P, Gomez P, Malfait M, Vereecke J. Intra- and intercellular Ca^{2+} signaling in retinal pigment epithelial cells during mechanical stimulation. *The FASEB Journal.* 1999; 13: 63–68. PMID: 9872930
5. Abu Khamidakh AE, Juuti-Uusitalo K, Larsson K, Skottman H, Hyttinen J. Intercellular Ca^{2+} wave propagation in human retinal pigment epithelium cells induced by mechanical stimulation. *Exp Eye Res.* 2013; 108: 129–139. doi: [10.1016/j.exer.2013.01.009](https://doi.org/10.1016/j.exer.2013.01.009) PMID: 23352832

6. Hansen M, Boitano S, Dirksen ER, Sanderson MJ. Intercellular calcium signaling induced by extracellular adenosine 5'-triphosphate and mechanical stimulation in airway epithelial cells. *Journal of Cell Science*. 1993; 106: 995–1004. PMID: [8126116](#)
7. Gelisken F, Inhoffen W, Partsch M, Schneider U, Kreissig I. Retinal pigment epithelial tear after photodynamic therapy for choroidal neovascularization. *Am J Ophthalmol*. 2001; 131: 518–520. PMID: [11292425](#)
8. Garg S, Brod R, Kim D, Lane RG, Maguire J, Fischer D. Retinal pigment epithelial tears after intravitreal bevacizumab injection for exudative age-related macular degeneration. *Clin Experiment Ophthalmol*. 2008; 36: 252–256. doi: [10.1111/j.1442-9071.2008.01710.x](#) PMID: [18412594](#)
9. Singh RP, Sears JE. Retinal pigment epithelial tears after pegaptanib injection for exudative age-related macular degeneration. *Am J Ophthalmol*. 2006; 142: 160–162. PMID: [16815269](#)
10. Rae Shi K. Revolution dawning in cardiotoxicity testing. *Nature Reviews Drug Discovery*. 2013; 12: 565–567. doi: [10.1038/nrd4083](#) PMID: [23903208](#)
11. Sneyd J, Tsaneva-Atanasova K, Bruce JIE, Straub SV, Giovannucci DR, Yule DI. A model of calcium waves in pancreatic and parotid acinar cells. *Biophys J*. 2003; 85: 1392–1405. PMID: [12944257](#)
12. Höfer T, Venance L, Giaume C. Control and plasticity of intercellular calcium waves in astrocytes: A modeling approach. *The Journal of Neuroscience*. 2002; 22: 4850–4859. PMID: [12077182](#)
13. Wu D, Jia Y, Zhan X, Yang L, Liu Q. Effects of gap junction to Ca²⁺ and to IP₃ on the synchronization of intercellular calcium oscillations in hepatocytes. *Biophys Chem*. 2005; 113: 145–154. PMID: [15617821](#)
14. Rizzolo LJ. Development and role of tight junctions in the retinal pigment epithelium. *Int Rev Cytol*. 2007; 258: 195–234. PMID: [17338922](#)
15. Appleby PA, Shabir S, Southgate J, Walker D. Cell-type-specific modelling of intracellular calcium signalling: A urothelial cell model. *Journal of The Royal Society Interface*. 2013; 10.
16. Warren NJ, Tawhai MH, Crampin EJ. Mathematical modelling of calcium wave propagation in mammalian airway epithelium: Evidence for regenerative ATP release. *Experimental Physiology*. 2010; 95: 232–249. doi: [10.1111/expphysiol.2009.049585](#) PMID: [19700517](#)
17. Dunn KC, Marmorstein AD, Bonilha VL, Rodriguez-Boulan E, Giordano F, Hjelmeland LM. Use of the ARPE-19 cell line as a model of RPE polarity: Basolateral secretion of FGF5. *Investigative Ophthalmology & Visual Science*. 1998; 39: 2744–2749.
18. Glotin A, Debacq-Chainiaux F, Brossas J, Faussat A, Tréton J, Zubielewicz A, et al. Prematurely senescent ARPE-19 cells display features of age-related macular degeneration. *Free Radical Biology and Medicine*. 2008; 44: 1348–1361. doi: [10.1016/j.freeradbiomed.2007.12.023](#) PMID: [18226607](#)
19. Yamamoto A, Akanuma S, Tachikawa M, Hosoya K. Involvement of LAT1 and LAT2 in the high- and low-affinity transport of L-leucine in human retinal pigment epithelial cells (ARPE-19 cells). *J Pharm Sci*. 2010; 99: 2475–2482. doi: [10.1002/jps.21991](#) PMID: [19890975](#)
20. Ablonczy Z, Dahrouj M, Tang PH, Liu Y, Sambamurti K, Marmorstein AD, et al. Human retinal pigment epithelium cells as functional models for the RPE in vivo. *Investigative Ophthalmology & Visual Science*. 2011; 52: 8614–8620.
21. Lemon G, Gibson WG, Bennett MR. Metabotropic receptor activation, desensitization and sequestration—I: Modelling calcium and inositol 1,4,5-trisphosphate dynamics following receptor activation. *J Theor Biol*. 2003; 223: 93–111. PMID: [12782119](#)
22. LeBeau AP, Yule DI, Groblewski GE, Sneyd J. Agonist-dependent phosphorylation of the inositol 1,4,5-trisphosphate receptor. *The Journal of General Physiology*. 1999; 113: 851–872. PMID: [10352035](#)
23. Keizer J, Levine L. Ryanodine receptor adaptation and Ca²⁺(-)induced Ca²⁺ release-dependent Ca²⁺ oscillations. *Biophys J*. 1996; 71: 3477–3487. PMID: [8968617](#)
24. Ahmado A, Carr A, Vugler AA, Semo M, Gias C, Lawrence JM, et al. Induction of differentiation by pyruvate and DMEM in the human retinal pigment epithelium cell line ARPE-19. *Investigative Ophthalmology & Visual Science*. 2011; 52: 7148–7159.
25. Dunn KC, Aotaki-Keen AE, Putkey FR, Hjelmeland LM. ARPE-19, a human retinal pigment epithelial cell line with differentiated properties. *Exp Eye Res*. 1996; 62: 155–170. PMID: [8698076](#)
26. Peng S, Rahner C, Rizzolo LJ. Apical and basal regulation of the permeability of the retinal pigment epithelium. *Investigative Ophthalmology & Visual Science*. 2003; 44: 808–817.
27. Ross MH, Romrell LJ, Kaye GI. *Histology a text and atlas*. Baltimore: Lippincott Williams & Wilkins; 1995.
28. Feeney-Burns L, Hilderbrand ES, Eldridge S. Aging human RPE: Morphometric analysis of macular, equatorial, and peripheral cells. *Investigative Ophthalmology & Visual Science*. 1984; 25: 195–200.

29. Wang J, Huang X, Huang W. A quantitative kinetic model for ATP-induced intracellular oscillations. *J Theor Biol.* 2007; 245: 510–519. PMID: [17188305](#)
30. Sullivan DM, Erb L, Anglade E, Weisman GA, Turner JT, Csaky KG. Identification and characterization of P2Y2 nucleotide receptors in human retinal pigment epithelial cells. *J Neurosci Res.* 1997; 49: 43–52. PMID: [9211988](#)
31. Giancoli DC. Physics for scientists and engineers with modern physics (3rd edition): Prentice Hall; 2000.
32. Fall CP, Marland ES, Wager JM, Tyson JJ. Computational cell biology. New York: Springer; 2002.
33. Chung W, Kermode JC. Suramin disrupts receptor-G protein coupling by blocking association of G protein α and $\beta\gamma$ subunits. *Journal of Pharmacology and Experimental Therapeutics.* 2005; 313: 191–198. PMID: [15626724](#)
34. Hamill OP. Twenty odd years of stretch-sensitive channels. *Pflugers Arch—Eur J Physiol.* 2006; 453: 333–351.
35. Luo Y, Zhuo Y, Fukuhara M, Rizzolo LJ. Effects of culture conditions on heterogeneity and the apical junctional complex of the ARPE-19 cell line. *Investigative Ophthalmology & Visual Science.* 2006; 47: 3644–3655.
36. Homolya L, Steinberg TH, Boucher RC. Cell to cell communication in response to mechanical stress via bilateral release of ATP and UTP in polarized epithelia. *The Journal of Cell Biology.* 2000; 150: 1349–1360. PMID: [10995440](#)
37. Reigada D, Mitchell CH. Release of ATP from retinal pigment epithelial cells involves both CFTR and vesicular transport. *American Journal of Physiology—Cell Physiology.* 2005; 288: C132–C140.
38. Mitchell CH. Release of ATP by a human retinal pigment epithelial cell line: Potential for autocrine stimulation through subretinal space. *The Journal of Physiology.* 2001; 534: 193–202. PMID: [11433002](#)
39. Reigada D, Lu W, Zhang X, Friedman C, Pendrak K, McGlinn A, et al. Degradation of extracellular ATP by the retinal pigment epithelium. *American Journal of Physiology—Cell Physiology.* 2005; 289: C617–C624.
40. Chaloux B, Caron AZ, Guillemette G. Protein kinase A increases the binding affinity and the Ca^{2+} release activity of the inositol 1,4,5-trisphosphate receptor type 3 in RINm5F cells. *Biology of the Cell.* 2007; 99: 379–388. PMID: [17373911](#)
41. Betzenhauser MJ, Fike JL, Wagner LE, Yule DI. Protein kinase A increases type-2 inositol 1,4,5-trisphosphate receptor activity by phosphorylation of serine 937. *Journal of Biological Chemistry.* 2009; 284: 25116–25125. doi: [10.1074/jbc.M109.010132](#) PMID: [19608738](#)
42. Caron AZ, Chaloux B, Arguin G, Guillemette G. Protein kinase C decreases the apparent affinity of the inositol 1,4,5-trisphosphate receptor type 3 in RINm5F cells. *Cell Calcium.* 2007; 42: 323–331. PMID: [17320950](#)
43. Wojcikiewicz RJH, Luo SG. Phosphorylation of inositol 1,4,5-trisphosphate receptors by cAMP-dependent protein kinase. *Journal of Biological Chemistry.* 1998; 273: 5670–5677. PMID: [9488697](#)
44. Nielsen MS, Nygaard Axelsen L, Sorgen PL, Verma V, Delmar M, Holstein-Rathlou N. Gap junctions. 2012;Jul; 2(3): 1981–2035. doi: [10.1002/cphy.c110051](#) PMID: [23723031](#)
45. Ye Z, Wyeth M, Baltan-Tekkok S, Ransom B. Functional hemichannels in astrocytes: A novel mechanism of glutamate release. *J Neurosci.* 2003;May 1; 23(9): 3588–3596. PMID: [12736329](#)
46. De Pittà M, Goldberg M, Volman V, Berry H, Ben-Jacob E. Glutamate regulation of calcium and IP₃ oscillating and pulsating dynamics in astrocytes. *J Biol Phys.* 2009; 35(4): 383–411. doi: [10.1007/s10867-009-9155-y](#) PMID: [19669422](#)
47. Guo C, Wang Y, Hu D, Han Q, Wang J, Hou X, et al. Modulation of migration and Ca^{2+} signaling in retinal pigment epithelium cells by recombinant human CTGF. *Current Eye Research.* 2009; 34:10: 852–862. doi: [10.3109/02713680903128935](#) PMID: [19895313](#)
48. Huang W, Wang L, Yuan M, Ma J, Hui Y. Adrenomedullin affects two signal transduction pathways and the migration in retinal pigment epithelial cells. *Investigative Ophthalmology & Visual Science.* 2004; 45: 1507–1513.
49. Savolainen V, Juuti-Uusitalo K, Onnela N, Vaajasaari H, Narkilahti S, Suuronen R, et al. Impedance spectroscopy in monitoring the maturation of stem cell-derived retinal pigment epithelium. *Annals of Biomedical Engineering.* 2011; 39: 3055–3069. doi: [10.1007/s10439-011-0387-1](#) PMID: [21904797](#)
50. Yang D, Elner SG, Clark AJ, Hughes BA, Petty HR, Elner VM. Activation of P2X receptors induces apoptosis in human retinal pigment epithelium. *Investigative Ophthalmology & Visual Science.* 2011; 52: 1522–1530.

51. Wimmers S, Halsband C, Seyler S, Milenkovic V, Strauss O. Voltage-dependent Ca²⁺ channels, not ryanodine receptors, activate Ca²⁺-dependent BK potassium channels in human retinal pigment epithelial cells. *Mol Vis.* 2008; 14: 2340–2348. PMID: [19096717](#)
52. Loeffler KU, Mangini NJ. Immunohistochemical localization of na+/Ca²⁺ exchanger in human retina and retinal pigment epithelium. *Graefe's Arch Clin Exp Ophthalmol.* 1998; 236: 929–933. PMID: [9865624](#)
53. Stalmans P, Himpens B. A decreased Ca²⁺-wave propagation is found among cultured RPE cells from dystrophic RCS rats. *Investigative Ophthalmology & Visual Science.* 1998; 39: 1493–1502.
54. Peterson WM, Megyesy C, Yu K, Miller SS. Extracellular ATP activates calcium signaling, ion, and fluid transport in retinal pigment epithelium. *The Journal of Neuroscience.* 1997; 17: 2324–2337. PMID: [9065493](#)
55. Maminishkis A, Jalilkee S, Blaug SA, Rymer J, Yerxa BR, Peterson WM, et al. The P2Y2 receptor agonist INS37217 stimulates RPE fluid transport in vitro and retinal reattachment in rat. *Investigative Ophthalmology & Visual Science.* 2002; 43: 3555–3566.
56. Siefjediers A, Hardt M, Prinz G, Diener M. Characterization of inositol 1,4,5-trisphosphate (IP₃) receptor subtypes at rat colonic epithelium. *Cell Calcium.* 2007; 41: 303–315. PMID: [16950509](#)
57. Maranto AR. Primary structure, ligand binding, and localization of the human type 3 inositol 1,4,5-trisphosphate receptor expressed in intestinal epithelium. *Journal of Biological Chemistry.* 1994; 269: 1222–1230. PMID: [8288584](#)
58. Sugiyama T, Yamamoto-Hino M, Wasano K, Mikoshiba K, Hasegawa M. Subtype-specific expression patterns of inositol 1,4,5-trisphosphate receptors in rat airway epithelial cells. *Journal of Histochemistry & Cytochemistry.* 1996; 44: 1237–1242.
59. Kennedy BG, Mangini NJ. Plasma membrane calcium-ATPase in cultured human retinal pigment epithelium. *Exp Eye Res.* 1996; 63: 547–556. PMID: [8994358](#)
60. Stalmans P, Himpens B. Confocal imaging of Ca²⁺ signaling in cultured rat retinal pigment epithelial cells during mechanical and pharmacologic stimulation. *Investigative Ophthalmology & Visual Science.* 1997; 38: 176–187.
61. Shen J, Gimbrone MA Jr, Luscinskas FW, Dewey CF Jr. Regulation of adenine nucleotide concentration at endothelium-fluid interface by viscous shear flow. *Biophys J.* 1993; 64: 1323–1330. PMID: [8494987](#)
62. Garrad RC, Otero MA, Erb L, Theiss PM, Clarke LL, Gonzalez FA, et al. Structural basis of agonist-induced desensitization and sequestration of the P2Y2 nucleotide receptor. *Journal of Biological Chemistry.* 1998; 273: 29437–29444. PMID: [9792648](#)
63. Mahama PA, Linderman JJ. A monte carlo study of the dynamics of G-protein activation. *Biophys J.* 1994; 67: 1345–1357. PMID: [7811949](#)
64. Fink CC, Slepchenko B, Loew LM. Determination of time-dependent inositol-1,4,5-trisphosphate concentrations during calcium release in a smooth muscle cell. *Biophys J.* 1999; 77: 617–628. PMID: [10388786](#)